Delft University of Technology

The effect of liquid co-flow on gas fractions, bubble velocities and chord lengths in bubbly flows. Part I

Uniform gas sparging and liquid co-flow

Muilwijk, Corné; Van den Akker, Harry E.A.

DOI
10.1016/j.ijmultiphaseflow.2020.103498

Publication date
2021

Document Version
Final published version

Published in
International Journal of Multiphase Flow

Citation (APA)
Muilwijk, C., & Van den Akker, H. E. A. (2021). The effect of liquid co-flow on gas fractions, bubble velocities and chord lengths in bubbly flows. Part I: Uniform gas sparging and liquid co-flow. *International Journal of Multiphase Flow*, *137*, Article 103498. https://doi.org/10.1016/j.ijmultiphaseflow.2020.103498

Important note
To cite this publication, please use the final published version (if applicable).
Please check the document version above.

Copyright
Other than for strictly personal use, it is not permitted to download, forward or distribute the text or part of it, without the consent of the author(s) and/or copyright holder(s), unless the work is under an open content license such as Creative Commons.

Takedown policy
Please contact us and provide details if you believe this document breaches copyrights.
We will remove access to the work immediately and investigate your claim.

This work is downloaded from Delft University of Technology.
For technical reasons the number of authors shown on this cover page is limited to a maximum of 10.

International Journal of Multiphase Flow 137 (2021) 103498

Contents lists available at ScienceDirect

International Journal of Multiphase Flow

journal homepage: www.elsevier.com/locate/ijmulflow

The effect of liquid co-flow on gas fractions, bubble velocities and chord lengths in bubbly flows. Part I: Uniform gas sparging and liquid co-flow

Corné Muilwijk[a,*], Harry E.A. Van den Akker[a,b]

[a] Bernal Institute, University of Limerick, V94 T9PX, Limerick, Ireland
[b] Transport Phenomena Lab, Department of Chemical Engineering, Delft University of Technology, Van der Maasweg 9, HZ Delft 2629, the Netherlands

ARTICLE INFO

Article history:
Received 8 April 2020
Revised 24 September 2020
Accepted 28 September 2020
Available online 24 October 2020

Keywords:
Bubble column
Bubble image velocimetry
Optical fibre probe
Liquid co-flow
Gas hold-up
Chord length distribution

ABSTRACT

Unique experiments were performed in a homogeneously sparged rectangular $400 \times 200 \times 2630$ mm ($W \times D \times H$) bubble column with and without liquid co-flow. Bubbles in the range 4–7 mm were produced by needle spargers, which resulted in a very uniform bubble size. Dual-tip optical fibre probes were used to measure horizontal profiles of gas fractions, bubble velocities and bubble chord lengths for superficial gas velocities U_{sg} in the range 0.63–6.25 cm/s and superficial liquid velocities U_{sl} up to 20 cm/s. Images of the bubble column were captured and a Bubble Image Velocimetry technique was adopted to calculate bubble (parcel) velocities. For low gas fractions, when a homogeneous flow regime occurred, both methods agreed very well and the optical fibre probes were found to be rather accurate for our bubbles. A liquid co-flow was found to have a calming effect and to stabilize a homogeneous bubbly flow regime, with less spatial variation in gas fractions and bubble velocities. Bubble chord lengths were almost normally distributed and do not exhibit the theoretical triangular probability density functions. The mean cord lengths were in the range 1.9–3.5 mm and found to increase with U_{sg} and to decrease slightly with increasing U_{sl}, while a liquid co-flow significantly reduced the standard deviation of the chord length distribution.

© 2020 The Authors. Published by Elsevier Ltd.
This is an open access article under the CC BY license (http://creativecommons.org/licenses/by/4.0/)

1. Introduction

Due to the continuous increase in computational power and demand for more accurate multiphase CFD simulations, there is an obvious need for more precise and detailed experimental data on bubbly flows for development and validation purposes. Euler-Euler CFD simulations, where both liquid and gas phases are modeled as interpenetrating fluids, require proper modeling of two-phase turbulence and of the interfacial forces such as drag, virtual mass, lift, wall lubrication and turbulent dispersion (Van den Akker, 1998; Van den Akker, 1998; Dhotre et al., 2013; Liao et al., 2015; Van Den Akker, 2015). These sub-models dealing with interfacial momentum transfer rates and bubble induced turbulence, are a strong function of (local) bubble size, slip velocity and void fraction. Many CFD models (see e.g. Dhotre et al., 2013) assume a constant, single bubble size to keep the computational burden of the simulation limited, while in experiments (mean) bubble size is usually badly controlled, reported or even known. Due to the many uncertainties in all these sub-models, this single bubble size then is often used (tacitly assumed or explicitly mentioned) as a tuning parameter (often in the range 4–6 mm) to construct a better agreement between simulations and experimental data, such as by Deen et al. (2001); Masood and Delgado (2014); Khan et al. (2017), and Rzehak et al. (2017).

However, in most bubble columns (industrial or for research purposes), bubbles are formed chaotically with a non-uniform distribution of poly-disperse bubbles; hence assuming a single bubble size to model interaction forces, dispersion and bubble induced turbulence is a bold oversimplification. A disparity of the (initial) bubble size (at gas sparger level) causes non-uniform bubble slip velocities, which leads to additional lateral dispersion (due to bubbles overtaking) generating additional turbulence, and strongly increased bubble collision rates, potentially leading to bubble coalescence and breakup (depending on the presence of surfactants). Bubble size distributions therefore play a vital role in setting up CFD simulations and in their validation (Besagni and Inzoli, 2016).

* Corresponding author.
E-mail addresses: corne_muilwijk@live.nl, Corne.Muilwijk@ul.ie (C. Muilwijk), Harry.VanDenAkker@ul.ie (H.E.A. Van den Akker).

https://doi.org/10.1016/j.ijmultiphaseflow.2020.103498
0301-9322/© 2020 The Authors. Published by Elsevier Ltd. This is an open access article under the CC BY license (http://creativecommons.org/licenses/by/4.0/)

Most recent developments of multi-phase CFD codes deal with breakup and coalescence kernels to more precisely model interfacial momentum transfer rates and bubble induced turbulence based on a local bubble size distribution (modeled by a population balance and a limited amount of bubble size classes), at the cost of increased complexity, longer simulation times and convergence issues. Huang et al. (2018) studied the impact of bubble size modeling in CFD simulations of bubble columns and found that: (1) the single bubble size models gave surprisingly good agreement with experimental data for symmetrical bubble columns, but less accurate agreement for a-symmetrically sparged configurations (which will be dealt with in Part II); and (2) there is no agreement on accurate models describing bubble coalescence and breakup rates (such as h- and i-MUSIG models). According to McClure et al. (2017) average bubble size and bubble size distribution have an effect on the swarm drag correction factor. Besagni et al. (2017) explored various approaches to represent the bubble size distribution and also concluded that the correct simulation of the fluid dynamics in the bubble column requires (more) accurate coalescence and break-up closures.

The rationale behind the research reported both in this Part I and in Part II is to acquire experimental data with bubble size as uniform as possible. Eventually, such data may be instrumental for distinguishing between effects caused by a swarm of uniform bubbles and the more complicated interactions between non-uniformly sized bubbles. In the latter case, more sophisticated models for coalescence and break-up are needed, see e.g. Mukherjee et al. (2019). In the ideal case of a single unique and constant bubble size, accounting for effects of a bubble size distribution and for breakup/coalescence is no longer necessary, such that a model for bubble induced turbulence may be validated independently of the enactment of models for interfacial momentum transfer.

It is then obvious that there is a coexisting requirement for bubble size measurements along with local bubble velocities and gas fractions. In this paper, we report new experimental data, in terms of local void fractions, bubble velocities and bubble chord lengths, on bubbly flows in a homogeneously sparged bubble column with a very uniform bubble size. For diluted bubbly flows (Besagni et al., 2016), or in shallow (pseudo 2D) bubble columns such as in Lau et al. (2013), an image analysis approach can be performed to obtain gas fractions and bubble size and shape measurements. For denser bubbly flows and/or larger bubble columns, image analysis becomes increasingly difficult due to overlapping bubbles. Measurement methods are then limited to X-ray densiometry (Hernandez-Alvarado et al., 2018; Mandalahalli et al., 2020), electrical resistance tomography (Singh et al., 2017) or intrusive measurement methods such as a borescope (Hernandez-Alvarado et al., 2018), wire-mesh sensors (Prasser et al., 1998; Hampel et al., 2009; Hernandez-Alvarado et al., 2018), shadowgraphic optical probes (Lichti and Bart, 2018), or (multi-point) electrical resistance (Buwa and Ranade, 2005; Singh et al., 2017) or optical fibre probes (Frijlink, 1987; Bakker, 1992; Harteveld, 2005).

Optical fibre or electrical resistance probes are regularly used in single tip, dual tip, or four-tip configurations.Probe signals are typically sampled at a rate in the order of $O(10^4)$ Hz (Chaumat et al., 2005; Le Corre et al., 2003; Shen and Nakamura, 2014), or sometimes even lower as long as the phase indicator function (PIF) can be registered with sufficient temporal resolution (Kiambi et al., 2003). Fibre probes in a single tip configuration are used to obtain the local phase indicator function (PIF) for determining the local gas fraction (Enrique Juliá et al., 2005) and the power spectral density of the PIF (Singh et al., 2017; Tyagi and Buwa, 2017). Dual-tip probes (with a vertical spacing Δy), can measure, in addition to the local PIF, bubble velocities (in the y-direction) based on the flying time and bubble diameters and chord lengths by assuming aligned uni-directional flow (Besagni et al., 2016; Frijlink, 1987; Bakker, 1992; Harteveld, 2005; Tyagi and Buwa, 2017; Groen, 2004; Simonnet et al., 2007; Dias et al., 2000; Barrau et al., 1999; Chaumat et al., 2005; Kiambi et al., 2003; Murzyn et al., 2005). Four-point probes (in a triangular pyramid (Guet et al., 2003; 2005; Ojha and Dahhan, 2018; Bai et al., 2008; Lucas and Mishra, 2005; Xue et al., 2003; Shen and Nakamura, 2014)) are adopted to also determine bubble velocity directions and shapes at the cost of a more complex algorithm for the probe signal analysis.

All these types of optical fibre probes are inherent to certain measurement inaccuracies and sampling bias caused by: (1) the blinding effect due to improper (de-)wetting of the probe; (2) the crawling effect as a result of deformation and/or deceleration of a pierced bubble; and (3) the drifting effect as bubble trajectories are altered due to the presence of an intrusive probe. The latter effect causes challenges for calculating correct flying times for dual-tip or four-point bubble probes as bubbles are deflected by the first (lower) probe tip and not measured by the upper probe tip(s).

While Cartellier (1992) correlated the rise time (or signal derivative as in Mizushima et al. (2013)) of a signal from a single optical fibre with interface velocity measurements from a digital camera, Cartellier and Barrau (1998a) used conical fiber tips and Frijlink (1987); Groen (2004); Cartellier and Barrau (1998b) introduced improved fibre tip shapes (as adopted later by Pjontek et al. (2014)) to determine the interface velocity. However, these authors still recommend calibration of the velocity measurements (using piercing experiments) for each manufactured tip or fluid.

More recent developments on velocity measurements using a single fibre are based on resolving the coherent beat frequency between the Fresnel reflection (fibre-fluid interface) and the reflections of an approaching interface by using a very high sampling rate (10 MHz) as in Chang et al. (2003); Lim et al. (2008). As this technique resolves the velocity of an approaching interface before bubble piercing takes place (when the distance between the fibre tip and bubble surface is 100–300 μm), effects of blinding, crawling and drifting are eliminated. However, as the intensity of the scattered light is limiting, velocity realizations are only found possible if the angle of attack is almost normal. Consequently, only as little as 2% of the detected bubbles contain velocity information (when pierced in the center of a bubble). While the velocity measurements may be still very representative, chord length measurements are largely biased for both single tip and dual tip optical fibres.

We now report new bubbly flow data acquired in the "LimBuRig" test facility, which is meticulously described in our previous paper (Muilwijk and Van den Akker, 2019). This setup, with its rectangular geometry for visualization purposes, has been developed with the view of generating experimental data for CFD validation and development. We opted for a rectangular configuration to facilitate visual observations and optical measurements since anyhow the test facility is intended to provide data for CFD validation rather than to mimic cases of direct industrial relevance. With the two separate inlet compartments, configurations with (a-)symmetric liquid and/or gas flow distributions can be studied and a wide range of operating conditions can be investigated; see also our Part II paper. A needle sparger was carefully constructed, such that a maximally uniform initial bubble size distribution of large bubbles in the range 4–7 mm (with an almost constant terminal rise velocity (Clift et al., 1978)) was achieved for U_{sg} up to 3.1 cm/s without liquid co-flow and beyond for higher co-flow velocities. In our previous study (Muilwijk and Van den Akker, 2019), a correlation was developed to describe the initial (volume equivalent) bubble size $d_{b,eq}$ (at gas sparger level) as a function of the superficial gas and liquid velocities. This correlation is used to calcu-

Table 1
Operating conditions. OFP: Optical Fibre Probe; BIV: Bubble Image Velocimetry. x: lateral position; y: vertical position (from trailing edge of the splitter plate). Note that the trailing edge of the splitter plate is located 17 cm above the sparger. Photographs, see Fig. 5, bubble velocity and chord length distributions (OPF measurements in the center of the column at $x = 0$ cm), see Figs. 9, and 14 respectively, are shown for four cases near the limits of the operating conditions ($U_{sg} = 1.25$, 6.25 cm/s and $U_{sl} = 0$, 20 cm/s).

Method	U_{sg} cm/s	U_{sl} cm/s	x cm	y cm	Fig.
OFPs (α, v_b, c)	0.63–6.25	0, 10, 20	−17.5 . . . 17.5 (in steps of 2.5 cm)	23, 63	Figs. 7, 8, 10, 11,12, 15, 16
BIV (v_b)	1.25	0, 10, 20	−20 . . . 20	−15 . . . 1250	Fig. 10b

late the bubble sizes in the present study. For bubbles in this size range, the terminal rise velocity (in contaminated water) is estimated as ≈ 24 cm/s according to the parameterization developed by Park et al. (2017).

We developed our in-house dual-tip optical fibre probes which were used to measure gas fractions, bubble velocities and bubble chord lengths. Bubble velocities measured with dual-tip optical fibre probes were then compared with bubble velocities measured using a Bubble Image Velocimetry (Cheng et al., 2005) approach at low gas fractions. Unlike other reported data on bubbly flow in the "pseudo-homogeneous" (poly-dispersed homogeneous) regime (Besagni et al., 2018), we report chord length distribution measurements for conditions with known (Muilwijk and Van den Akker, 2019) uniform single sized bubbles for various U_{sg} and U_{sl}.

The main objectives of this paper are to show how: (1) the (uniformity of) the gas fraction α is a function of the superficial liquid and gas velocities and to validate the previously proposed correlation for the gas hold-up; (2) the bubble velocity v_b is influenced by liquid co-flow, where the optical fibre probe (OFP) and Bubble Image Velocimetry (BIV) methods are compared; and (3) the distribution of the bubble chord length c is a function of the superficial gas velocity and liquid co-flow velocity and how they relate to the mean bubble diameter.

The structure of this paper is then as follows. Section 2 briefly describes the setup and adopted measurement methods; Section 3 shows results on the measured void fractions, bubble velocities and chord lengths respectively; and conclusions and recommendations for future work are presented in Section 4.

2. Experimental

2.1. Test facility

Fig. 1 shows a schematic of the apparatus used for this study. Two parallel streams of bubbly flows, for this work with equal superficial gas, U_{sg}, and superficial liquid velocities, U_{sl}, start interacting downstream of the trailing edge of a splitter plate. The depth of the channel D is 0.2 m and the width W of the channel is $2D = 0.4$ m. The superficial velocities U_{sg} and U_{sl} are the independent variables, defined as volumetric flow rates (at $P_0 = 1.013$ bar and $T = 20\,^{\circ}$C) divided by the cross-sectional area of the column. U_{sg} was varied in the range 0.63–6.25 cm/s, and U_{sl} in the range 0–20 cm/s. Bubbles are formed by $2 \times 14^2 = 392$ ø1.55 mm i.d. needles to establish formation of a uniform homogeneously distributed bubble size. More details on the design of the test facility, overall gas fractions (using a bed expansion technique) and bubble formation rates/diameters can be found in our previous paper (Muilwijk and Van den Akker, 2019). Optical Fibre Probes and a Bubble Image Velocimetry technique are used to study the flow. These techniques are discussed below and the experimental settings are summarized in Table 1.

2.2. Bubble image velocimetry

Images of the bubble column (of the area annotated with BIV in Fig. 1) were captured at a rate of 100 and 120 Hz (Jai Go 2400 M camera, Kowa LMVZ166HC 16–64 mm varifocal lens) and corrected for lens distortion, see Fig. 2a. The camera was calibrated using both the width and height of the column and resulted in a spatial resolution of 0.70 mm/pix. A contrast limited adaptive histogram equalization (CLAHE) algorithm (Zuiderveld, 1994) was used to improve the contrast of the images as shown in Fig. 2b. A direct image cross-correlation technique as in Cheng et al. (2005) was adopted to obtain the velocity of bubble parcels.

The image cross-correlation coefficient between f (time t) and g (time $t + \Delta t$) was calculated according to

$$R_{i,j} = \frac{\Sigma_m \Sigma_n \left[f(m+i, n+j) - \overline{f} \right] [g(m,n) - \overline{g}]}{\sqrt{\Sigma_m \Sigma_n \left[f(m,n) - \overline{f} \right]^2 \Sigma_m \Sigma_n [g(m,n) - \overline{g}]^2}} \tag{1}$$

where n, m are sub-ranges (interrogation windows) of the full image and i, j are the pixel shifts in vertical and horizontal direction. Fig. 3 shows a surface plot of $R_{i,j}$ as function of i and j. A window size of 32×32 pixels (120 Hz image acquisition rate) or 40×40 pixels (100 Hz) was found as an optimal compromise between spatial resolution and correlation intensity. A window overlap of 50% was used, which resulted in a spatial resolution (half window size) of ≈ 1.25–1.5 cm. Quadratic interpolation was used to obtain a sub-pixel displacement resolution and spurious velocities were removed using a mean $\pm 3\sigma$ outlier detection algorithm.

2.3. Dual-tip optical fibre probes

Horizontal profiles of gas fraction α, bubble velocity v_b, and bubble chord length c were measured in the center of the column (between front and rear wall, see Fig. 1) at 23 and 63 cm downstream of the trailing edge of the splitter plate (40 and 80 cm above the sparger level) by using two in-house developed double-point optical fiber probes.

The probe response signals from each probe tip were sampled with a NI USB-6001 I/O device at a rate of 5 kHz per channel, and the signals were normalized using the span of a signal (see black and grey curve in Fig. 4). It was found that the adopted acquisition rate is sufficient to record the phase indicator functions, as multiple points were sampled on the steep parts of the signal (when tip (de-)wetting takes place). In order to determine the threshold intersections with a higher temporal resolution, the signals were upsampled at a rate of 20 kHz using quadratic interpolation and binarized to obtain the phase indicator functions, using a threshold value of 3× the standard deviation of the baseline noise (red dashed line).

Void fractions were then calculated using the average value of the phase indicator functions for the lower probe tips, as those are less subjected to the drifting effect. A measurement duration of 100 s was found to be sufficient to obtain an accurate estimate of the local void fraction.

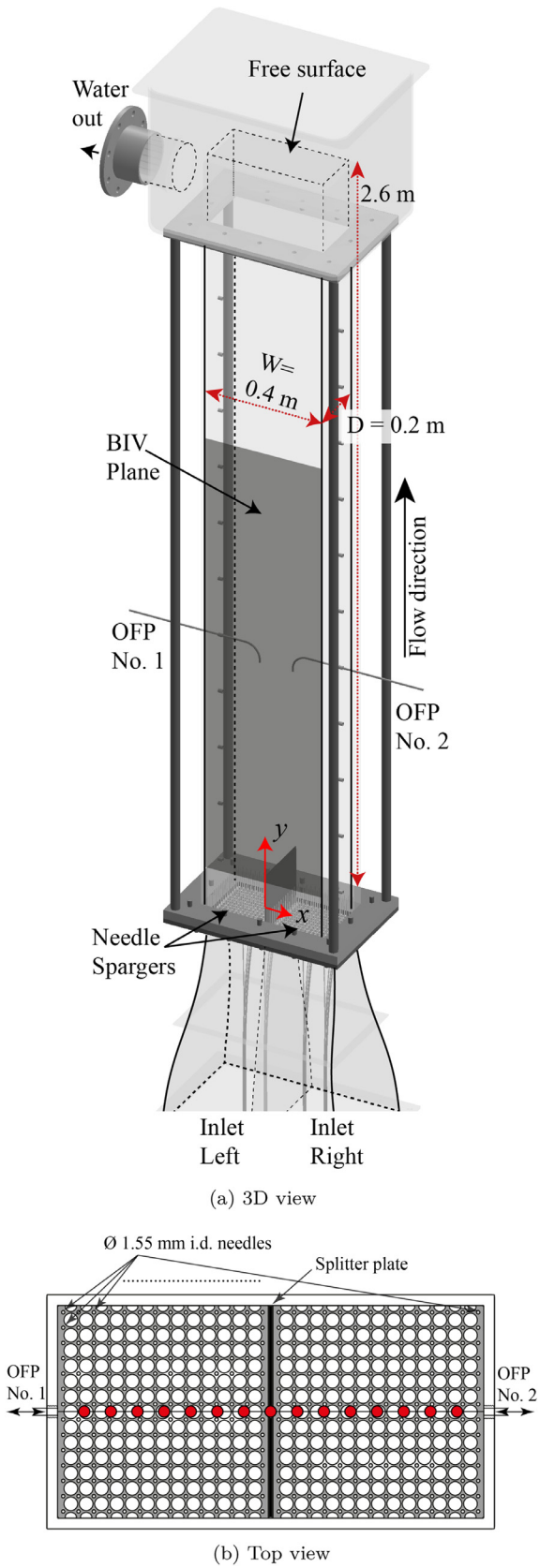

Fig. 1. Schematic drawing of the bubbly flow channel. Bubbles are formed on top of the needle spargers and air is separated from the water at the free surface. The Optical Fibre Probes (at a height of 40 and 80 cm above the needle spargers) are traversed in the x-direction along the center line of the column in steps of 2.5 cm, see red markers in (b). The needle sparger level, at $y = 0$, is located 17 cm below the trailing edge of the splitter plate located. The experimental conditions are summarized in Table 1.

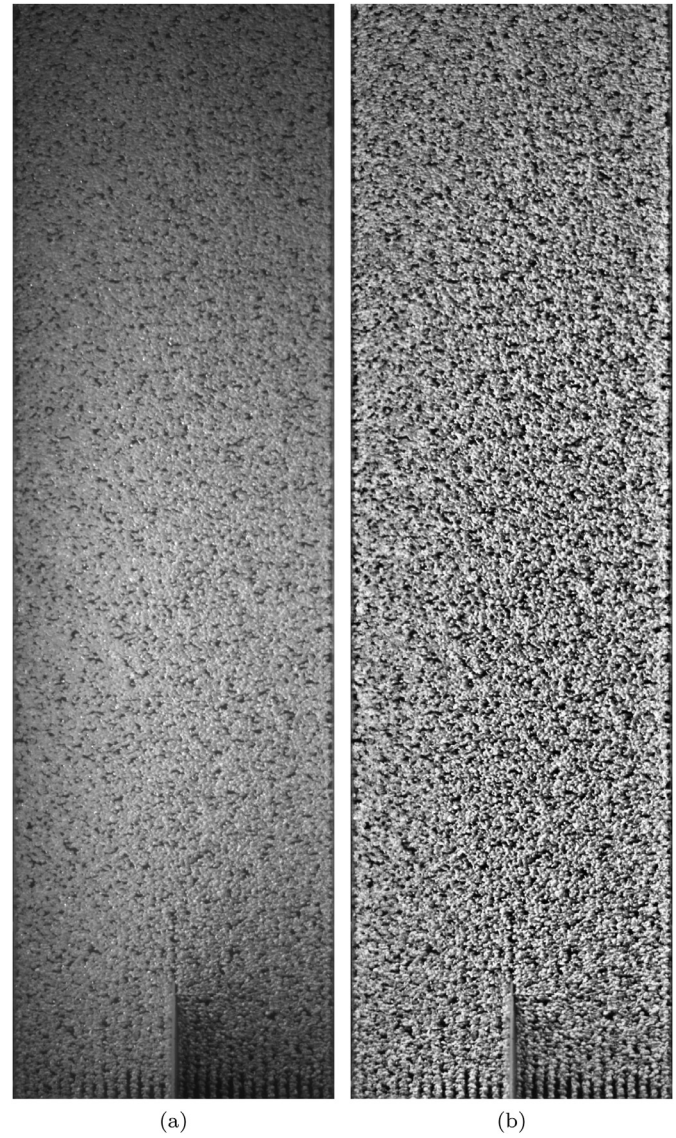

Fig. 2. Images of the bubble column. The field of view is 40×140 cm ($W \times H$), starting ≈ 2 cm above the needle sparger. (a) Raw image corrected for lens distortion. (b) Enhanced image using a contrast-limited adaptive histogram equalization (CLAHE) technique. $U_{sg} = 1.67$ cm/s. $U_{sl} = 0.2$ m/s.

The direct cross correlation between the phase indicator functions from the upper and lower fibre tips was computed to obtain the time lag $\tau_{\max}$ between the signals. Then, for each bubble detected on the lower fibre tip at time t^i (▲), a matching crenel is searched on the upper fibre tip signal within a time interval $[t^i + a\tau_{\max}; t^i + b\tau_{\max}]$ as in Chaumat et al. (2005). The value of a was set as 0.5 and b was chosen in the range 2.5–6, dependent of the gas fraction.

The velocity of a bubble i traveling through both lower and upper tips, is then calculated according to

$$v_b^i = \frac{\Delta y}{\Delta t_f^i} \tag{2}$$

where the flying time Δt_f^i, is measured as the time the ith bubble front interface takes to rise from the lower to the upper fibre tip as indicated in Fig. 4a.

The vertical distance between the two tips of a probe, Δy, was 3.75 mm for probe No. 1 and 2.45 mm for Probe No. 2. As we expect uniform large ($d_{eq} > 4$ mm) oblate/wobbling bubbles rising

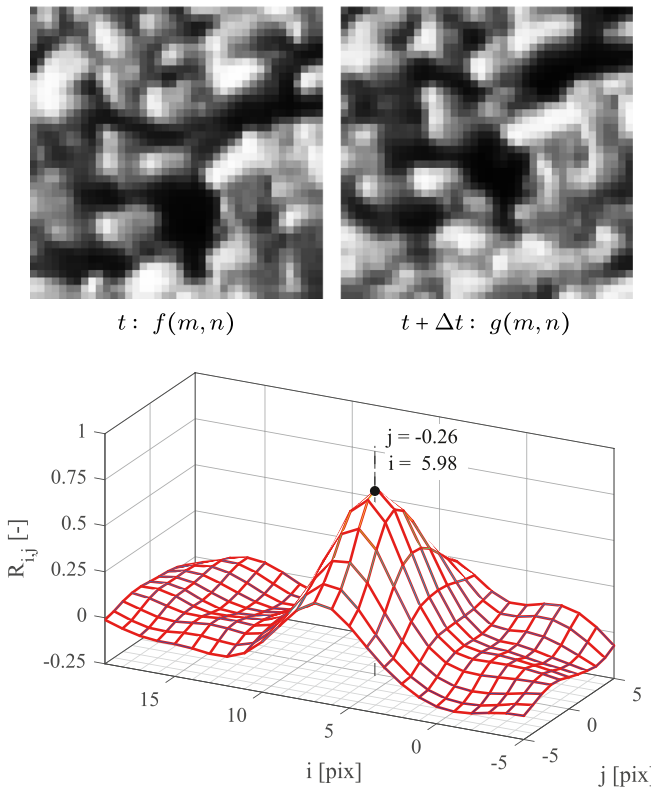

Fig. 3. Top: Interrogation windows $f(m,n)$ (at time step t) and $g(m,n)$ (at time step $t+\Delta t$), with m,n being $2.8 \times 2.8\,\text{cm}^2$ sub ranges ($40 \times 40\,\text{pix}^2$) of the full image shown by Fig. 2b. Bottom: Image cross correlation coefficient $R_{i,j}$ between f and g as a function of the pixel shifts i, j, see Eq. (1).

mostly vertically, the probe tip separations Δy and sampling rate were optimized to deliver accurate results and no significant difference was found between the two dual-tip probes. For our application, bubble velocities > 1.0 m/s are highly unlikely and a sufficient resolution in the velocity domain is achieved with our optical fibre probes.

The dwelling time t_d^i is the duration a probe tip spends inside a bubble (time between the piercing of the front and rear interface of a bubble, see Fig. 4). Fig. 4b shows histograms of the relative dwell time difference $\Delta t_d^i / < t_d^i >$, where $\Delta t_d^i = t_{d,l}^i - t_{d,u}^i$ and $< t_d^i > = (t_{d,l}^i + t_{d,u}^i)/2$, where the subscripts l, u refer to the lower and upper fibre tip, respectively. Under ideal probe conditions (rigid ellipsoidal bubbles, no crawling, no drifting), it is assumed that this parameter exhibits a uni-modal distribution for bubbles traveling with a lateral velocity component.

Hence, a value of 1.2 was adopted for the pairing criterion (see dashed lines in Fig. 4b as the probability density function estimate of the pairing parameter was found to have a minimum at approximately 1.2. Bubble pairs not passing the pairing criterion, with an absolute relative dwell time difference exceeding the value of 1.2, were ascribed to extreme drifting and crawling.

Barrau et al. (1999) studied the effect of relaxing the pairing criterion on the resulting phase averaged gas velocity and found no significant difference when the pairing rate (percentage of bubbles detected on the lower tip matched to a crenel on the upper tip signal) exceeded 20%. Fig. B.19 shows the pairing rates for our experiments for further reference.

The phase weighed mean bubble velocity (phasic gas velocity) is then calculated as:

$$\overline{v_b} = \frac{\Sigma_{i=1}^{N} t_d^i v_b^i}{\Sigma_{i=1}^{N} t_d^i} \tag{3}$$

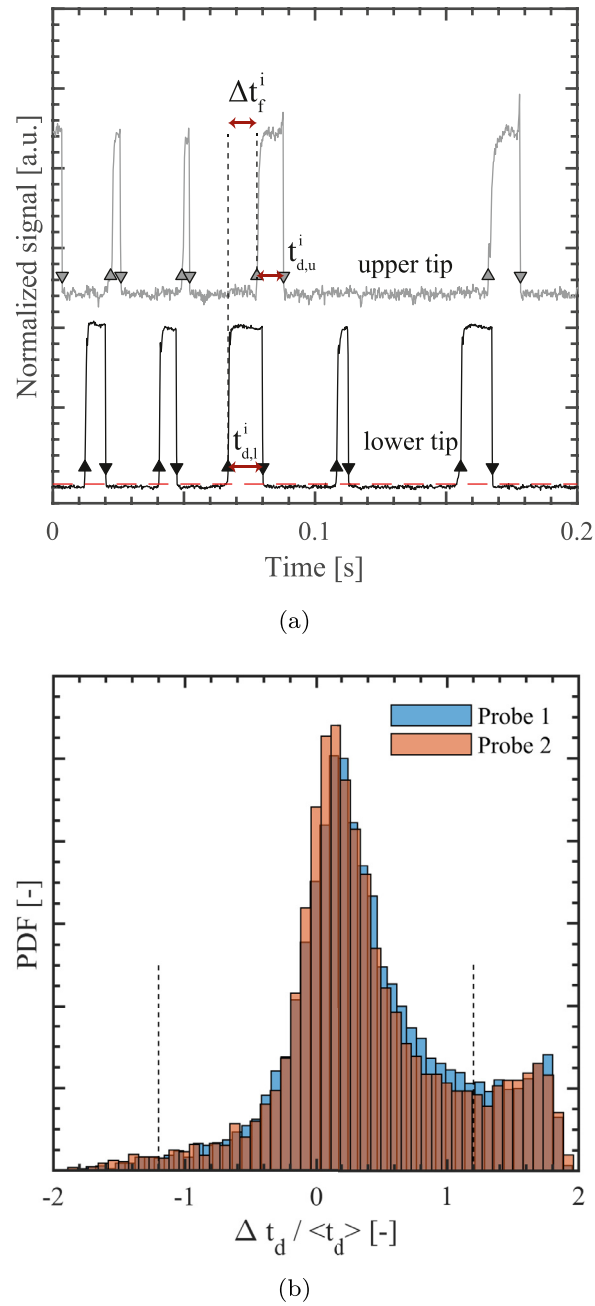

Fig. 4. (a) Normalized dual-tip optical fibre probe signal. Black: lower tip; Grey: upper tip. Δt_f : Flying time; t_d: Dwelling time; i: bubble count. The red horizontal dotted line shows the binarization threshold. (b) Histograms of the relative dwelling times for a bubble measured on the lower and upper fibre tips. The pairing criterium is set at ± 1.2, where a local minimum of the histogram is observed. The red bars show the measurements obtained by probe 1, whereas the blue bars denote the measurements of probe 2 (color online).

where N is the validated amount of bubbles measured on both fibre tips passing the pairing criterion.

For each valid bubble velocity measurement, the chord length of a bubble is then calculated according to:

$$c^i = t_d^i v_b^i \tag{4}$$

The mean and standard deviation of the chord length was then calculated from the chord length distribution and denoted as $\bar{c}$ and Stdev(c)

The mean chord length can also be calculated according to Chaumat et al. (2005); Lim et al. (2008)[1]:

$$\bar{c} = \frac{\alpha v_{mp}}{f_b} \tag{5}$$

where v_{mp} is the most probable velocity, calculated as $\Delta y/\tau_{\max}$ and f_b is the bubble detection rate on the lower fiber tip, which can be determined with high accuracy. Both methods for determining $\bar{c}$ will be compared in Section 3.

For spherical and (oblate) ellipsoidal bubbles, the mean vertical diameter of the bubbles $d_{\parallel}$ can be calculated according to Simonnet et al. (2007); Colombet et al. (2015):

$$d_{\parallel} = \frac{3}{2}\bar{c} \tag{6}$$

Assuming uniformly sized bubbles, the volume equivalent bubble diameter then relates to the aspect ratio and vertical diameter of the bubbles according to Besagni et al. (2016); Simonnet et al. (2007); Colombet et al. (2015):

$$d_{b,eq} = d_{\parallel}\varphi^{-2/3} = d_{\perp}\varphi^{1/3} \tag{7}$$

where the aspect ratio of the bubble $\varphi = d_{\parallel}/d_{\perp}$, with $d_{\perp}$ and $d_{\parallel}$ being the major and minor axes of an oblate ellipsoidal bubble.

3. Results & discussion

3.1. Visual observations

Fig. 5 shows photographs of the bubble column for four operating conditions in the studied range, e.g. $U_{sg} = 1.25$ (left) and 6.25 cm/s (right) and co-flow velocities $U_{sl} = 0$ (top) and 0.2 m/s (bottom). Videos of the bubble column under these conditions are given in the Supplementary Material.

At low aeration rates (left), the gas fraction is low (5.5% (a) and 3% (c)) and the column is sufficiently optically accessible to obtain a good contrast for image analysis. Individual bubbles can be distinguished and a very uniform bubble size distribution is observed. A BIV technique may be used in this regime due to the justified assumption of uniformity of the flow (the absence of wall/center peaking in velocity and/or void fraction), while the effects of front and rear wall on the measured velocity profiles are ignored.

At intermediate to high gas fractions, a boundary layer develops at both sides of the splitter plate, thereby creating a wake region in the center of the bubble column, leading to horizontal gradients of the void fraction and bubble velocities in the center of the column.

At high aeration rates (right) the fluid is opaque, $\alpha = 24\%$ (b) and 14% (d), and only bubbles in the front wall region can be recorded on a camera. Bubbles do not follow organized rectilinear bubble paths (see also Fig. 6), and a three dimensional turmoil develops as clearly visible in the videos in the Supplementary Material. Back-mixing occurs, while a center peaking void fraction/bubble velocity and flow reversal at the column walls is emerging. Under these conditions, a BIV technique cannot be used anymore as the assumption of quasi-2D flow (no gradient in the collinear direction) no longer holds.

Without liquid co-flow and high aeration rates (Fig. 5b), the uniformity of the bubble size distribution suffers due to coalescence occurring during bubble formation at the needles (see sparger region). With increasing liquid co-flow (Fig. 5d), coalescence (e.g. at the needle) was prevented (liquid co-flow reduces bubble-bubble interactions (Muilwijk and Van den Akker, 2019a))

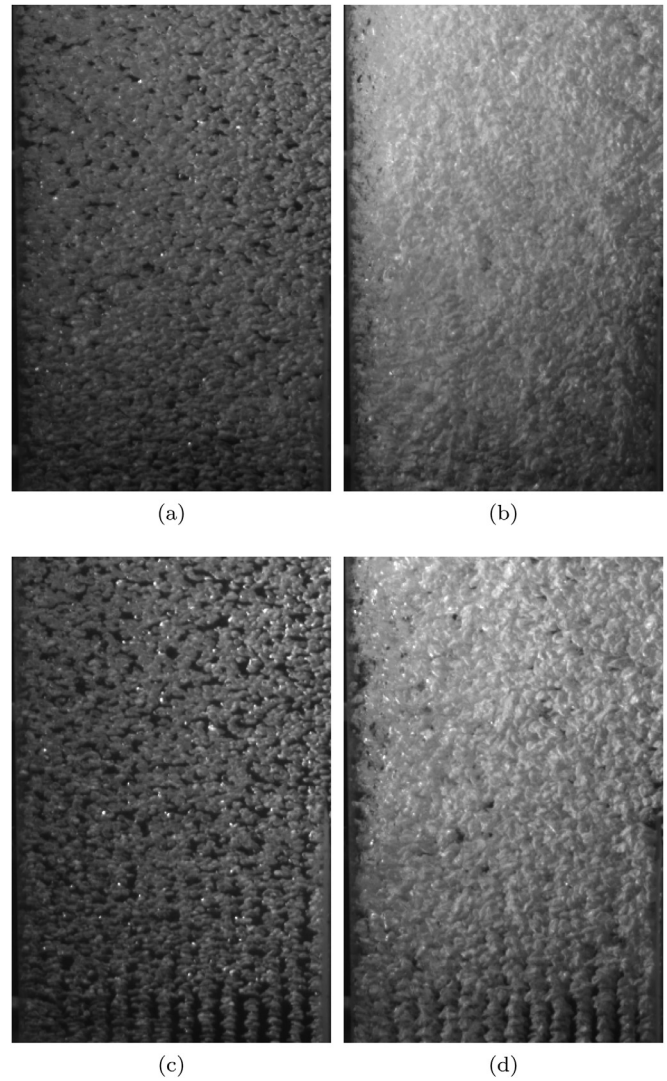

Fig. 5. Close-up photographs of the left inlet compartment of the bubble column (full frame videos given in the Supplementary Material). The width of the photos are 20 cm. Top: $U_{sl} = 0$ m/s; bottom: $U_{sl} = 0.2$ m/s (flow direction up). Left: $U_{sg} = 1.25$ cm/s; right: $U_{sg} = 6.25$ cm/s. (a): $\alpha \approx 5.5\%$, $d_{b,eq} = 5.1$ mm; (b): $\alpha \approx 24\%$, $d_{b,eq}$ poly-disperse due to coalescence; (c): $\alpha \approx 3.0\%$, $d_{b,eq} = 4.4$ mm; and (d): $\alpha \approx 14\%$, $d_{b,eq} = 7.1$ mm. The bubble rise velocity for bubbles in this size range is approximately constant at 24 cm/s (Park et al., 2017).

and a uniform bubble size distribution was reestablished. Parallel trains of bubbles were formed in the sparger region, which started to interact some 5–10 cm above the needle outlets, also leading to the development turbulent structures and backmixing.

Fig. 6 shows simulated bubble streaks by averaging the 500 photographs of a 5 s image series. Under typical conditions our column is free from lateral dispersion, at least in the lower part of the column as the rise velocities of our bubbles are very uniform thanks to the already limited variation in bubble size. At low superficial gas velocities (Fig. 6a), bubble streaks originating from a single needle can be distinguished up to a height of ≈ 20 cm above the needle outlets, while a wake effect of the splitter plate is clearly visible in the center of the column. For somewhat higher U_{sg} (Fig. 6b, see also Fig. 5a), lateral dispersion is emerging and separate bubble streaks cannot be observed beyond ≈ 5–10 cm above the needle outlets. A coflow (Fig. 6c) was then found to reduce lateral dispersion due to a strong advection as straight bubble streaks can be detected up to ≈ 40 above the needle outlets, see also Fig. 5c.

[1] Note that the factor $\frac{3}{2}$ in Eq. (6) in Simonnet et al. (2007) for the calculation of $d_{\parallel}$ out of $\overline{v_b}, \alpha$ and f_b is erroneous.

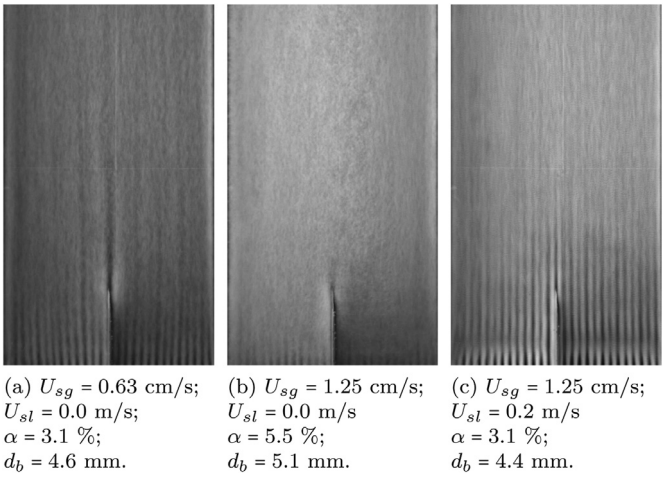

Fig. 6. Bubble streaks obtained by a 5s simulated long exposure (image averaging technique). Corrected for lens distortion and contrast enhanced using a CLAHE technique. See Supplementary Material for the videos. The width of the images is 40 cm. Each inlet has an array of 14 × 14 needles.

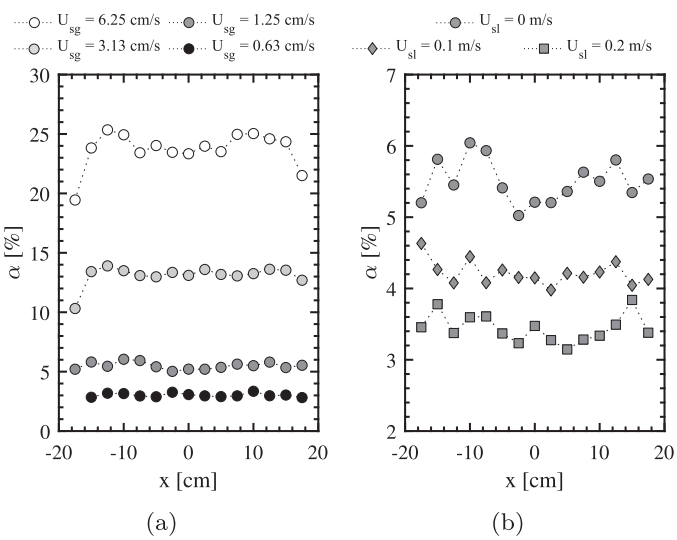

Fig. 7. Gas fraction α as a function of horizontal position x for (a) various superficial gas velocities U_{sg} without liquid co-flow and (b) for various superficial liquid velocities U_{sl} for U_{sg} = 1.25 cm/s. y = 80 cm.

3.2. Gas fraction

3.2.1. Horizontal gas fraction profiles

Fig. 7a shows lateral profiles of the void fraction for U_{sg} in the range 0.63–6.25 cm/s without co-flow at a height of 80 cm above the sparger level. For low gas flow rates, the gas fraction profile was very uniform, whereas for increasing gas flow rates, steep gradients of α were found in the close vicinity of the column wall. Due to wall effects (including splitter plate), bubbles migrated to the center of the bubble column, thereby creating local maxima in the void fraction profile and liquid downflow in the direct vicinity of the column walls.

Fig. 7b shows lateral profiles of the void fraction for U_{sl} in the range 0–0.2 m/s for U_{sg} = 1.25 cm/s (note the difference in scale between (a) and (b)). While a slightly uneven void fraction profile was observed for U_{sl} = 0 m/s (grey ●), a liquid co-flow flattens the void fraction profile and the effect of the splitter plate and wall effects on the lateral bubble migration were reduced.

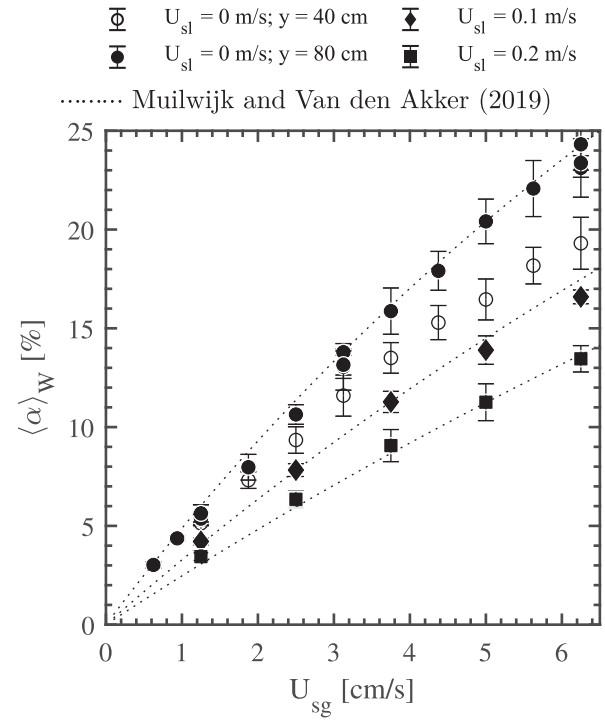

Fig. 8. Void fraction $\langle\alpha\rangle$ as a function of superficial gas velocity setting U_{sg}. The error bars denote the spreading of α in horizontal direction. The dotted line shows the predicted overall gas hold-up as calculated using our previously developed correlation (Muilwijk and Van den Akker, 2019). The open markers show the results at y = 40 cm; the solid black markers show the data of y = 80 cm.

3.2.2. Gas hold-up curves

Fig. 8 shows the development of the horizontally averaged void fraction profiles $\langle\alpha\rangle_W$ as a function of the superficial gas velocity for U_{sl} = 0 (●, ○), 0.1 (♦), and 0.2 m/s (■), where the subscript W refers to the averaging over the width of the column, e.g. the 15 measurements locations as shown in Fig. 1b. The error bars denote the span wise variation of α in the void fraction profiles as shown in Fig. 7. The filled markers denote measurements at a height of 80 cm above the sparger level, while the open markers show measurements at a height of 40 cm. Measurements at U_{sg} = 1.25, 3.13 and 6.25 were repeated thrice and were found be reproducible.

For higher U_{sg} and for U_{sl} = 0 m/s, lower void fractions were measured at y = 40 cm compared to the measurements at y = 80 cm. This can be explained by a more homogeneous flow pattern closer to the sparger, in the developing region of the bubble column, as a center-peaking void fraction profile with liquid downflow at the walls is emerging.

It should be noted that U_{sg} on the x-axis is given as the setting at standard conditions while the actual superficial gas velocity is a function of the height in the column. More data is required in terms of local pressure measurements to derive the local gas flux as a function of the height in the column.

The dotted lines in Fig. 8 show the overall gas hold-up as predicted by the correlation developed in our previous study (Muilwijk and Van den Akker, 2019), which was obtained through bed expansion experiments. Good agreement was achieved with void fraction measurements using optical fibre probes (markers) at a height of 80 cm above the sparger. A comprehensive comparison of our gas hold-up curves with data found in the literature is given in our previous paper (Muilwijk and Van den Akker, 2019). It was found that gas hold-up curves are highly case-specific, which is also clearly illustrated by a thorough overview of gas hold-up

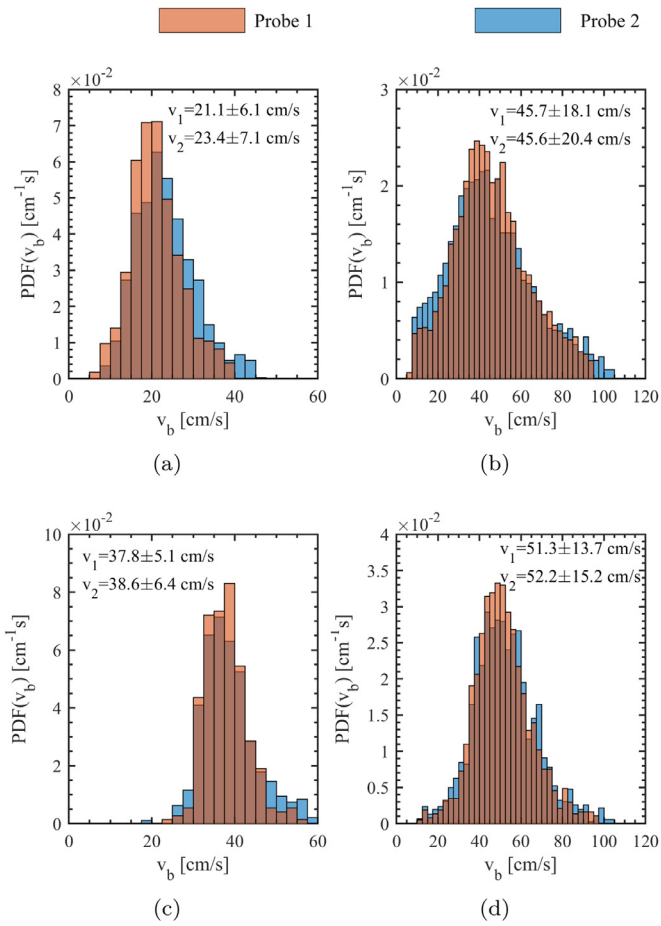

Fig. 9. Velocity histograms measured by the optical fibre probes in the centre of the column (x=0) at $y = 80$ cm. Top: $U_{sl} = 0$ m/s; Bottom: $U_{sl} = 0.2$ m/s. Left: $U_{sg} = 1.25$ cm/s; Right: $U_{sg} = 6.25$ cm/s.

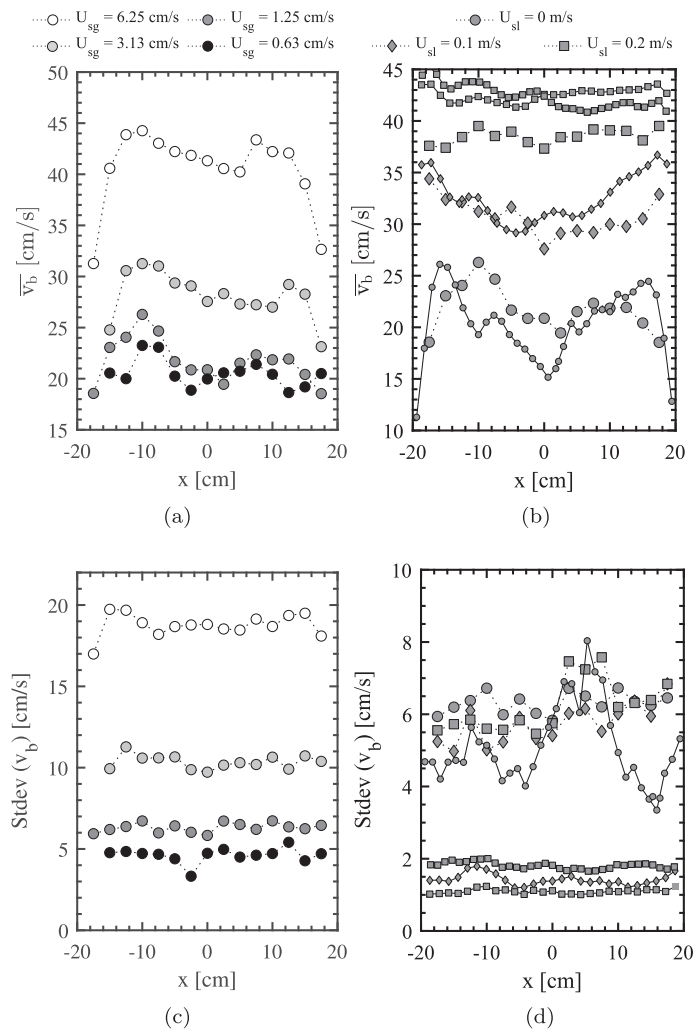

Fig. 10. (a,b) Mean bubble velocities $\overline{v_b}$ and (c,d) standard deviations of the bubble velocities Stdev(v_b) as a function of horizontal position x at $y = 80$ cm. Left (a,c): no co-flow ($U_{sl} = 0$ m/s) and various U_{sg} (OFP measurements only); Right (b,d): with co-flow ($U_{sl} = 0, 0.1, 0.2$ m/s) for $U_{sg} = 1.25$ cm/s. The larger markers denote the OFP data, whereas the smaller markers show the BIV results (the series with a higher x-resolution show data obtained with and image acquisition rate of 120 Hz, and the series with a lower x-resolution represent BIV results based on images captured at a rate of 100 Hz). Videos of the column for the conditions in (b,d) are given in the Supplementary Material.

curves given in Gandhi and Joshi (2010). As such, it can be concluded that gas hold-up curves are a strong function of the bubble size and sparging method (initial bubble size distribution). Many drift-flux correlations, for estimating the gas hold-up, ignore the effect of the bubble size distribution and may thus give inaccurate predictions.

3.3. Bubble velocities

3.3.1. Bubble velocity histograms

Fig. 9 shows velocity histograms for four operating conditions in the range studied, e.g. $U_{sg} = 1.25$ (left) and 6.25 cm/s (right) and co-flow velocities $U_{sl} = 0$ (top) and 0.2 m/s (bottom). For all cases, the velocity histograms exhibited an almost Gaussian distribution. As bubbles were almost uniform in size and had an almost equal rise velocity in this size range (Clift et al., 1978), the spreading of the measured velocities can be explained by: (1) swarm effects, as bubbles may be hindered or accelerated due to the presence of other bubbles, thereby developing large circulation patterns; (2) interface oscillations, as bubbles of this size behave as wobbling bubbles (instead of rigid ellipsoids); (3) crawling, as the velocity of an interface may be influenced by the presence of the probe and may also depend on the bubble velocity itself, interface curvature (phase of oscillation) and piercing position; (4) coalescence at gas sparger level, when the uniformity of the initial bubble size is compromised (only for high U_{sg} and no liquid co-flow, see Fig. 9b). For increasing liquid co-flow the spread in bubble velocities narrows as bubbles carry more momentum (in their added mass) and are less likely to suffer from crawling and swarming.

3.3.2. Horizontal profiles of the bubble velocity

Fig. 10a shows lateral profiles of the mean bubble velocity $\overline{v_b}$ for U_{sg} in the range 0.63–6.25 cm/s without co-flow at a height of 80 cm above the sparger level. Low gas flow rates resulted in slightly wavy bubble velocity profiles with bubble velocities in the range 19–24 cm/s. For increasing gas flow rates, bubbles traversed away from the column side walls (and splitter plate), thereby creating two maxima in the bubble velocity profiles. Steep gradients of $\overline{v_b}$ show up in the vicinity of the column wall with bubbles even moving downward close to the column side walls, which cannot be properly detected using optical fibre probes in the current configuration.

Standard deviations of the bubble velocity (see Fig. 10c) are almost constant across the lateral direction and increase with increasing U_{sg}. Slight increases of Stdev(v_b) are noticed close to the

column wall for high U_{sg} due to the emerging, unsteady, down flux at the column walls.

Fig. 10b shows lateral profiles of $\overline{v_b}$ obtained using OFPs (large markers + dotted line) and our BIV technique (small markers + solid line) for U_{sl} in the range $0-0.2$ m/s and $U_{sg} = 1.25$ cm/s. The shape of the velocity profiles, obtained by using the two methods, is comparable for all cases, while for $U_{sl} = 0.1$ m/s the agreement is almost perfect.

Due to wake effects of the splitter plate, a double peaking bubble velocity profile develops for $U_{sl} = 0$ m/s (grey ●). A liquid co-flow then has a uniforming effect on the bubble velocity profile as (1) the effect of the splitter plate and wall effects on the lateral bubble migration is reduced as bubbles are entrained by a (uniform) liquid flow and (2) rather lower standard deviations (see Fig. 10d) of the bubble velocity are measured with increasing U_{sl}.

For $U_{sl} = 0$ m/s (higher α), BIV showed lower bubble velocities than the OFPs, which may be due to a gentle down flux reducing the bubble velocities in the vicinity of the column walls. For $U_{sl} = 0.2$ m/s, velocities from BIV were ≈9% higher than mean velocities obtained by using the dual-tip optical fibre probes. BIV experiments at $U_{sg} = 1.25$ cm/s were repeated twice. Whereas images were initially acquired at a frame rate of 100 Hz, a different set of experiments was carried out with a framerate of 120 Hz. No significant differences were found between the experiments for $U_{sl} > 0$ m/s, as the flow patterns without co-flow were found to be very sensitive to small inaccuracies of the gas flow rates in the left and right inlet, which is further studied in our Part II paper. The discrepancies between OFP and BIV may be due to 3-D effects (wall peaking of the gas fraction and bubble velocity profiles).

Shen et al. (2016, 2017); Sun et al. (2014) observed wall peaking of the void fraction in the near vicinity ($< 10-20$ mm distance) of the column walls as a function of the gas flux. This near-wall regions are outside the reach of the bubble probes. A future investigation, with a different probe design, should be dedicated to zoom-in on the phenomena happening in the near vicinity of the side or front walls. A wall peaking void fraction may explain the higher bubble velocities from the BIV captured in the near-wall region. Experiments with a smaller depth of view, higher frame rate and improved homogeneous illumination are recommended to optimize the BIV technique.

3.3.3. Bubble velocities as a function of U_{sg}

We now average the mean bubble velocities and standard deviations measured on the 15 lateral positions as shown in Fig. 1b. Fig. 11a shows plots of this center-line averaged mean bubble velocity $\langle\overline{v_b}\rangle_W$ as a function of superficial gas velocity. The error bars in Fig. 11a are a measure of the uniformity of the profiles of $\overline{v_b}$ (in Fig. 10a,b) as a result of center peaking velocity profiles. Fig. 11b shows the related (also center-line averaged) standard deviation of the bubble velocities $\langle \mathrm{Stdev}(v_b)\rangle_W$, which are a measure of the temporal fluctuations of v_b.

Without liquid co-flow (●, ○), average mean bubble velocities increase with increasing superficial gas velocity up to $U_{sg} \approx 3.0$ cm/s. An almost constant average mean bubble velocity was measured in the range $U_{sg} = 3.0-4.5$ cm/s, whereafter the bubble velocities rapidly increase with increasing U_{sg}.

The standard deviation of the bubble velocities continuously increases with increasing superficial gas velocity for the whole range of U_{sg}. Higher bubble velocities and standard deviations were measured at a height of $y = 80$ cm (●), compared to $y = 40$ cm (○), as the flow regime gradually departed from a homogeneous bubbly flow and center peaking void fraction and bubble velocity profiles started to develop. While at the lowest aeration rates, bubbles in the range $4-8$ mm essentially have a constant rise velocity of ≈ 24 cm/s (Clift et al., 1978), a standard deviation of ≈ 5 cm/s was

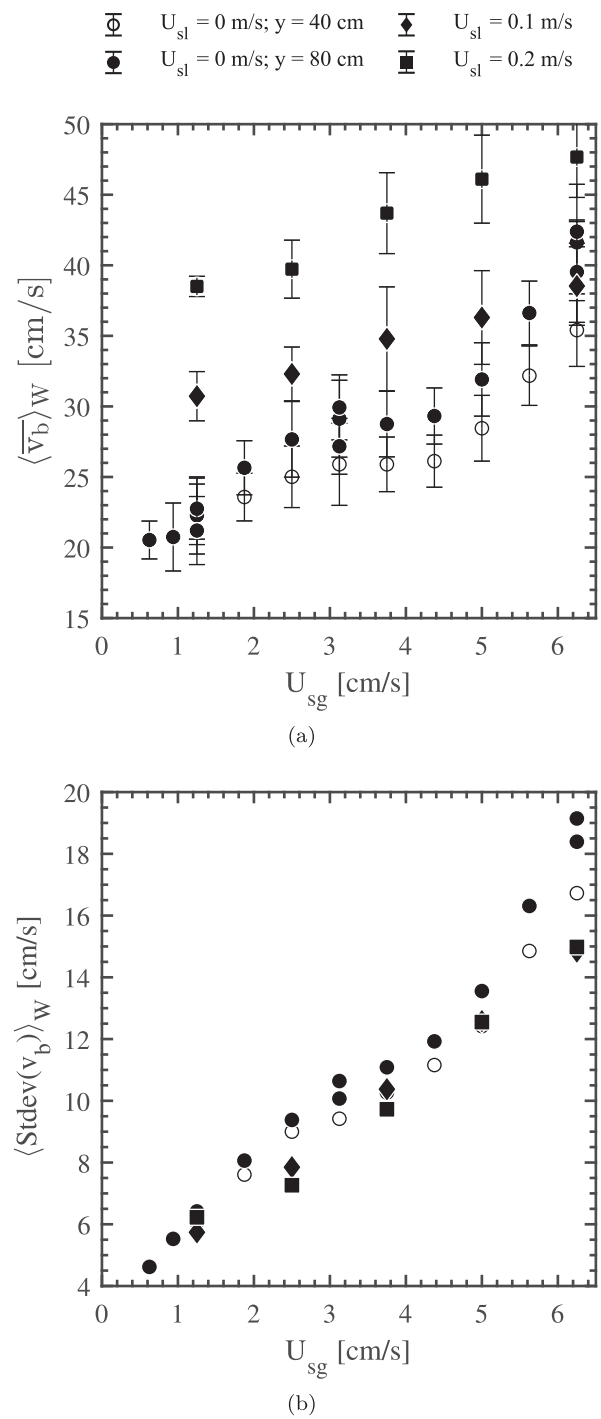

Fig. 11. (a) Time and horizontally averaged bubble velocities $\langle\overline{v_b}\rangle$ and (b) standard deviations of v_b as a function of the superficial gas velocity setting. The error bars denote the spread in (a) $\overline{v_b}$ and (b) $\mathrm{Stdev}(v_b)$ with respect to the horizontal direction. The open markers show the results at $y = 40$ cm; the solid black markers show the data for $y = 80$ cm.

found in our study and ascribed to interface oscillations and crawling. At higher aeration rates, swarm effects and coalescence effects give rise to the increase in $\mathrm{Stdev}(v_b)$

For cases with liquid co-flow, higher bubble velocities (at low/intermediate U_{sg}) were observed which increased almost linearly with increasing superficial gas velocities. No shoulder followed by a steep increase was detected at intermediate/high U_{sg}. Also, co-flow leads to lower standard deviations of v_b (see Fig. 11b)

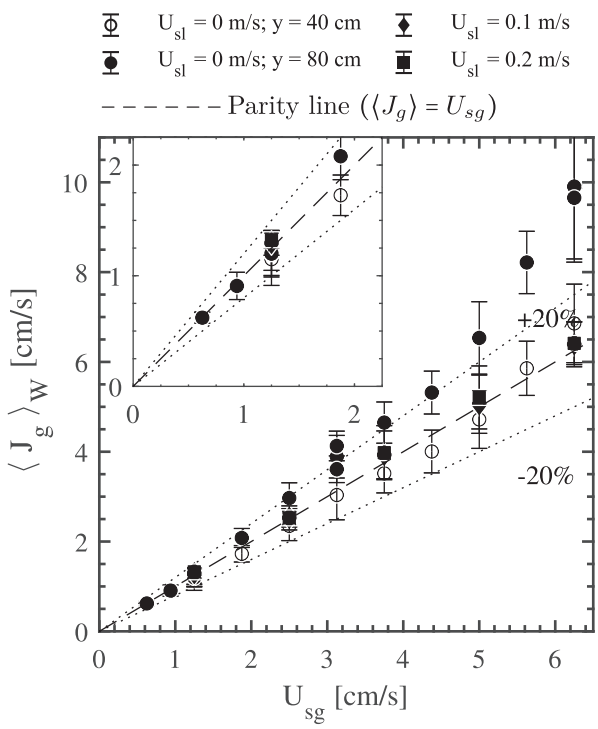

Fig. 12. Measured gas flux $\langle J_g \rangle$, see Eq. (8), as a function of applied superficial gas velocity setting. The dashed line shows the parity line. The solid markers show data taken at $y = 80$ cm; the open markers show data for $y = 40$ cm.

and the lateral spreading thereof, indicating that there is no (gradual) regime transition, as the homogeneous bubbly flow regime is stabilized by the liquid co-flow.

3.3.4. Gas flux measurements

The local gas flux, as measured by the optical fibre probes, can be calculated as $\alpha\overline{v_b}$, where the phasic quantity $\overline{v_b}$ is the phase averaged bubble velocity as per Eq. (3). The centerline averaged gas flux $\langle J_g \rangle_W$, along the accessible positions along the column center line, is then given by:

$$\langle J_g \rangle_W = \frac{1}{x_R - x_L} \int_{x_L}^{x_R} \alpha \overline{v_b} dx \tag{8}$$

and shown in Fig. 12. The $\langle\rangle$ brackets denote spatial averaging of the locations shown in Fig. 1b. The closest position the probes can travel to the wall is 2.5 cm, hence, $x_L = -17.5$ and $x_R = 17.5$ cm. Under ideal circumstances, in a uniform homogeneous bubbly flow, the measured $\langle J_g \rangle_W$ equals the U_{sg} as calculated from the gas flow rate settings.

Bai et al. (2010); Shen et al. (2016) used $\langle J_g \rangle$ to assess the accuracy of the bubble probes, whereas (Colombet et al., 2015) adopted $\langle J_g \rangle$ to show the degree of homogeneity of the bubbly flow. While Bai et al. (2010) found their $\langle J_g \rangle$ being some 30% smaller than the applied gas flow rate (for $2 < U_{sg} < 10$ cm/s), we found quite good agreement between both values for U_{sg} up to about 2 cm/s without co-flow. At higher U_{sg}, the measured gas flux departs from the applied U_{sg} which can be explained by the center peaking void fraction and bubble velocity profiles (with down flow emerging at the column walls). This divergence starts at $U_{sg} = 2.0$ cm/s and becomes increasingly distinct for $U_{sg} > 4.5$ cm/s, while this effect is less prominent for the region closer to the sparger where the flow pattern is still developing (open ○).

The change in hydrostatic pressure between the two measurement planes, at $y = 40$ and $y = 80$ cm ($\Delta H = 0.4$ m), can be approximated by $\rho_W g \Delta H(1 - \alpha)$. This was found to be less than 4% of the atmospheric pressure, hence the difference in local superficial gas velocity between $y = 40$ and $y = 80$ cm does not explain the difference in $\langle j_g \rangle_W$ we measure between $y = 40$ and $y = 80$ cm for $U_{sg} > 3$ cm/s. No significant difference of the pairing rate was found between the measurements taken at $y = 40$ cm and $y = 80$ cm, see also Fig. B.19, hence the bubble probes at both heights work equally well.

Our measured gas fluxes $\langle J_g \rangle_W$, for $U_{sl} = 0$ m/s at $y = 80$ cm, are higher as (1) more measurements were performed in the bulk of the column (the plateau in the void fraction and velocity profiles, see Figs. 7a and 10 a respectively); and (2) very low/negative bubble velocities in the vicinity of the column wall cannot be measured due to the limitations of the probe.

The measurements at $y = 40$ cm were taken closer to the sparger, still in the developing region of the bubble column, and follow the parity line due to a still rather uniform bubbly flow. In the developed region of the bubble column, liquid downflow at the side walls emerged, leading to a center-peaking gas fraction/bubble velocity profile, hence, $\langle J_g \rangle_W$ departs from this parity line. Considering data valuable for CFD validation, centreline profiles would give systematic and valuable information on the bubble flow behavior.

It should be noted that U_{sg} on the x−axis is at standard conditions, while the measured $\langle J_g \rangle$ is at a higher pressure. Therefore, a somewhat lower measured gas flux $\langle J_g \rangle_W$ can be expected due to the higher gas density. Measurements of the local pressure or gas fraction distribution along the height of the column are required to properly account for the change in gas fraction difference. In case a liquid co-flow is applied, the gas flux is almost equal to the applied U_{sg} for all cases considered. It may then be concluded that (1) the dual-tip bubble probes work very well for determining α and $\overline{v_b}$; (2) the flow regime gradually departs from homogeneous bubbly flow at $U_{sg} > 2.0$ cm/s and $U_{sl} = 0$ m/s; and (3) a liquid co-flow stabilizes the homogeneous bubbly flow regime.

3.3.5. Literature comparison

Fig. 13 shows the relative bubble (slip) velocity as a function of the gas fraction, where U_s is calculated assuming uniform (co-)flow by using a drift-flux model according to Muilwijk and Van den Akker (2019):

$$U_s = \langle \overline{v_b} \rangle_W - \frac{U_{sl}}{1 - \langle \alpha \rangle_W} \tag{9}$$

The black markers represent the data as shown in Figs. 8 and 11 a, whereas the colored markers and dashed line show relative gas velocities as a function of α as reported in a selection of relevant literature.

While the relative gas velocities reported by Colombet et al. (2015); Alméras et al. (2018); Besagni et al. (2016) (no co-flow) and Garnier et al. (2002); Simonnet et al. (2007) (with co-flow) show decreasing gas velocities with increasing gas fraction at low gas fractions, we found U_s to increase with increasing α for all conditions ($\alpha > 3\%$) investigated. As the estimated terminal rise velocity U_t for isolated bubbles in the range 4–8 mm is ≈ 24 cm/s, U_s at low α was slightly smaller than U_t. Hindered rise (as in Besagni et al., 2016 up to $\alpha \approx 5\%$ and Simonnet et al. (2007) up to $\alpha \approx 15\%$) may occur to a some extent for lower gas fractions, but no data could be obtained in that regime due to the risk of weeping. The early onset of swarming (increasing U_s with increasing α) can thus be explained by the large bubble size in agreement with Simonnet et al. (2007), as small (uniform) bubbles, which stabilize homogeneous bubbly flow, show hindered bubble rise behavior as in Garnier et al. (2002); Alméras et al. (2018); Colombet et al. (2015).

Relative velocities measured with the optical probes are higher than derived from global gas hold-up measurements by using a drift-flux model as in Muilwijk and Van den Akker (2019) (see

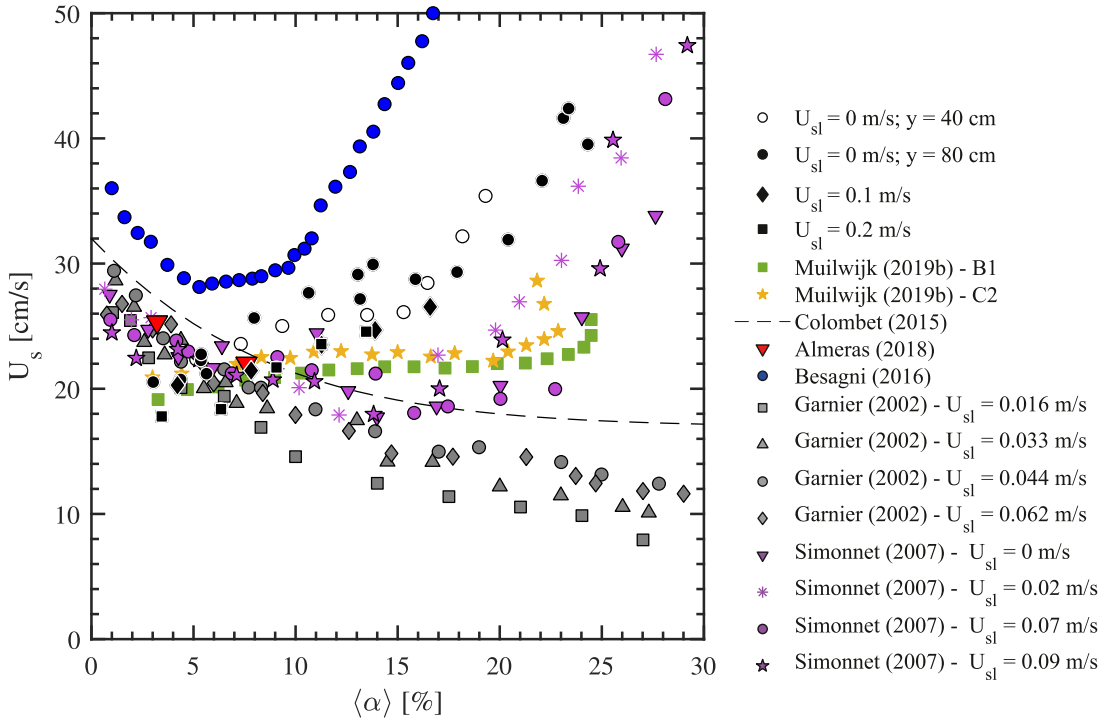

Fig. 13. Relative gas (slip) velocity U_s as a function of gas fraction. A comparison with relevant reported data. The present data follows from Eq. (9), with $\langle\alpha\rangle$ and $\langle\overline{v_b}\rangle$ from Figs. 8 and 11(a) respectively.

cases B1, C2 in Fig. 13). At low α (uniform bubbly flow), good agreement was found, but, due to a center peaking gas fraction/bubble velocity profile at higher void fractions, the measured gas flux is overestimated (see Fig. 12). U_s is then also overestimated as the probes are biased to high (upward) velocities and low (downward) velocities in the vicinity of the column wall cannot be measured by the current probe configuration.

It was observed that when a liquid co-flow was applied, it reduces the emerging down-flow at the wall as the liquid entrained by the bubble wakes can overflow from the top of the column, thereby resulting in a more homogeneous flow. A critical value of U_{sl} may exist when the liquid flow rate (U_{sl}) equals the liquid entrainment rate in the bubble wakes, which is roughly estimated at $C_{AM}U_{sg}$, with C_{AM} being the added mass coefficient. More experiments, at lower co-flow rates will be required to investigate this hypothesis.

3.4. Bubble chord lengths

3.4.1. Histograms of bubble chord length distributions

Fig. 14 shows chord length distributions for four operating conditions in the studied range, e.g. $U_{sg} = 1.25$ (left) and 6.25 cm/s (right) and co-flow velocities U_{sl}= 0 (top) and 0.2 m/s (bottom). Bubble chord lengths clearly increase with increasing gas flow rates (left to right), while mean chord lengths become slightly smaller and distributions more narrow with increasing co-flow velocity (top to bottom). A small shoulder shows up at the left tail for $U_{sl} = 0$ m/s, which is not present for chord length distributions obtained for (higher) co-flow velocities, which agrees well with the bubble contours presented in Muilwijk and Van den Akker (2019a), indicating that liquid co-flow tends to make the bubble more spherical.

Roig et al. (1998) found a similar chord length distribution as shown in Fig. 14a, while bubbles were produced by porous tube spargers, which typically results in a polydisperse bubble size distribution. Constant bubble chord length distributions were found

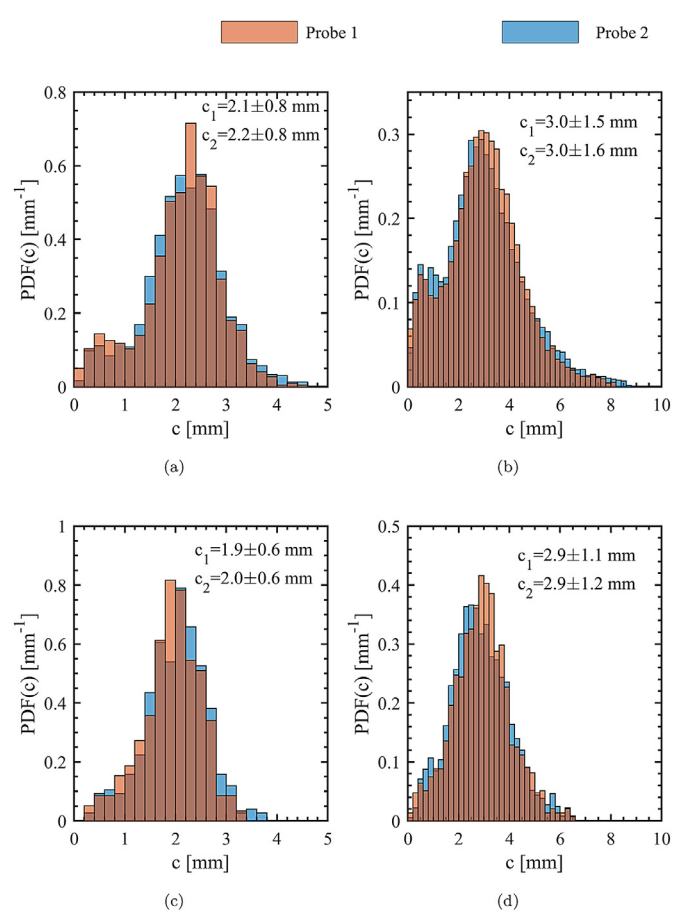

Fig. 14. Chord length distributions measured by the optical fibre probes in the centre of the column ($x = 0$) at $y = 80$ cm. Top: $U_{sl} = 0$ m/s; Bottom: $U_{sl} = 0.2$ m/s. Left: $U_{sg} = 1.25$ cm/s; Right: $U_{sg} = 6.25$ cm/s.

across the lateral and streamwise position and they concluded that "either break-up and coalescence did not occur in the flows, or they were in mutual equilibrium." While their chord length distribution was found to be independent of the superficial liquid velocity, where $c = 2.1 \pm 0.6$ mm for α =1.9% and $U_{sl} = 0.2$–0.5 m/s, our results presented in Fig. 14 show a clear dependence of c on U_{sl} and U_{sg} as per the design of the needle sparger (Muilwijk and Van den Akker, 2019).

A theoretically derived triangular left skewed chord length distribution for rigid ellipsoidal (uniform) bubbles (Liu and Clark, 1995; Clark and Turton, 1988), with the largest measured chord length being the maximum (vertical) diameter $d_{\|}$, was not observed in our cases. Also Chaumat et al. (2005) reported that 15% of the measured chord length values were larger than the maximum diameter obtained from image analysis. Although our previous paper (Muilwijk and Van den Akker, 2019) shows that very uniform bubbles are formed at gas sparger level for U_{sg} up to 3 cm/s (and beyond when a liquid co-flow is applied), theoretically predicted triangular chord length histograms were not recovered. This discrepancy is explained by: (1) probe biases with respect to piercing position; and (2) the wobbling behavior (as clearly visualized in the Supplementary material of Ref. Muilwijk and Van den Akker (2019)) of non-rigid bubbles, which also explains the longer right tail for larger bubbles (see Fig. 14c).

Theoretical chord length distributions were simulated (see A.1) for mono-disperse rigid and wobbling bubbles, as well as for a poly-disperse bubble mixture and we found very similar chord length distributions for mono-disperse wobbling bubbles and poly-disperse rigid (oblate) bubbles. Therefore, we refrain from performing a transformation from a chord length distribution to a bubble size distribution as in Besagni et al. (2016); Hoang et al. (2015) as assuming a constant ellipsoidal shape renders such a transformation invalid. A more complex method should be developed to account for a variable bubble shape when transforming chord length distributions into a bubble size distributions as a constant oblate ellipsoidal shape is proven invalid for large bubbles.

3.4.2. Lateral profiles of the mean bubble chord lengths

Fig. 15 shows lateral profiles of the mean chord lengths $\bar{c}$ (top) and standard deviations Stdev(c) of the chord length distribution at a height of 80 cm above the sparger level for (a,c) U_{sg} in the range 0.63–6.25 cm/s without co-flow; and (b,d) U_{sl} in the range 0–0.2 m/s for $U_{sg} = 1.25$ cm/s (note the difference in scale between the left and right column). While the void fraction and bubble velocity profiles are clearly non-uniform for some of these cases (see Figs. 7 and 10), a very constant mean chord length $\bar{c}$ was observed for almost all U_{sg} and U_{sl}, which indicates that the bubble size (distribution) is very constant over the cross section of the column. A slight spanwise spreading was found for lower gas fractions, as smaller bubbles are more subjective to drifting and the number of valid bubble measurements decreased.

3.4.3. Bubble chord lengths as a function of U_{sg}

Fig. 16a plots the centerline averaged mean bubble chord length $\langle\bar{c}\rangle_W$ as a function of the applied superficial gas velocity and Fig. 16b shows the related (spatially averaged) standard deviation $\langle\text{Stdev}(c)\rangle_W$ of the bubble chord lengths. The error bars indicate the lateral spreading of $\bar{c}$ and Stdev(c) respectively.

No significant difference was found between chord lengths measured at $y = 80$ cm and $y = 40$ cm (latter not shown), which indicates that the bubble size (distribution) is independent of the vertical position. The averaged mean chord lengths $\langle\bar{c}\rangle$ (a) and the standard deviation thereof (b) increase with increasing U_{sg} for cases with and without liquid co-flow. Whereas the lateral spread

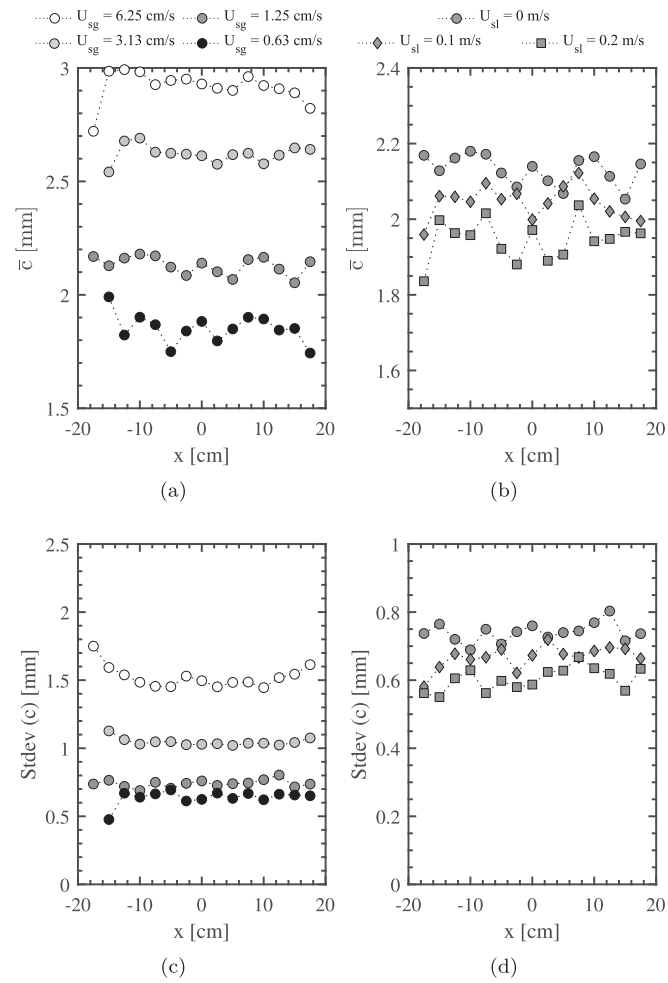

Fig. 15. Top: Mean chord lengths as a function of horizontal position x at $y = 80$ cm. Bottom: Standard deviations of the chord length distributions as a function of x. (a,c): Various gas flow rates without liquid co-flow; (b,d): Various superficial liquid velocities at $U_{sg} = 1.25$ cm/s.

(error bars) of both $\langle\bar{c}\rangle_W$ and $\langle\text{Stdev}(c)\rangle_W$ is almost independent of U_{sg}, these distributions become narrower with increasing co-flow velocity, which confirms that liquid co-flow has an organizing effect on the (homogeneous) bubbly flow and the bubble formation process.

The open markers (Fig. 16a) show the average chord length $\bar{c}$ as calculated by Eq. (5). Compared to the mean of the chord length distributions (solid markers, Eq. (4)), these chord lengths are somewhat overestimated as they depend on the direct cross correlation between the lower and upper fibre tip signal, which are biased to the larger (vertical) velocities. While α and f_b can be obtained with a high degree of accuracy (Chaumat et al., 2005), it should be noted that (mean) chord length measurements are subject to a similar relative error as bubble velocity measurements, see Eqs. (4) and (5).

A clear bend in the slope of $\langle\bar{c}\rangle_W$ is observed at $U_{sg} \approx 2.5$–3 cm/s (without liquid co-flow), which coincides with the apparent transition from single separate bubble formation to bubble formation with coalescence at the needle. As smaller satellite bubbles may split off from bubbles formed at the needle sparger and a uniform single bubble size cannot be assumed beyond $U_{sg} \approx 3.1$ cm/s (Muilwijk and Van den Akker, 2019), a smaller chord length is expected, which agrees well with the trend in Fig. 16a and the chord length histogram in Fig. 14b.

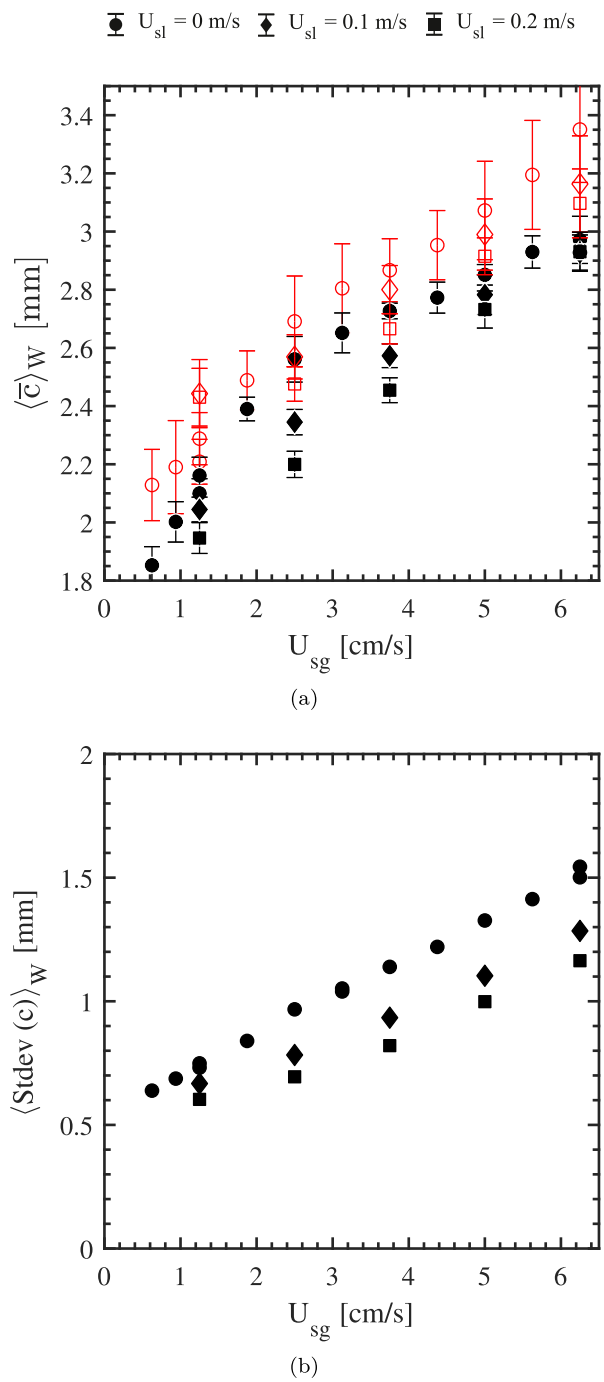

Fig. 16. (a) Mean bubble chord lengths $\langle\bar{c}\rangle$ and (b) standard deviations of c as a function of superficial gas velocity setting for $y = 80$ cm. The error bars denote the spread of $\bar{c}$ and Stdev(c) in horizontal direction. The solid markers (a) show the mean of the chord length distributions (Eq. (4)), whereas the open markers show the average chord length as calculated from the local gas flux and the bubble detection rate (Eq. (5)).

While still assuming a uniform volume equivalent bubble size and an average oblate ellipsoidal shape, the mean aspect ratio of a bubble may be calculated using Eqs. (6) and (7). $d_{b,eq}$ was then calculated as a function of U_{sg} and U_{sl} using a correlation developed in our previous study (Muilwijk and Van den Akker, 2019) and the volume equivalent bubble diameter was found to be in the range of 4–8 mm ($2.2 < Eo < 8.7$).

The calculated bubble aspect ratios φ were in the range 0.4–0.55 (see A.2). This agrees quite well with the values (≈ 0.5) reported in Garnier et al. (2002); Riboux et al. (2010) for the smaller bubble size. The aspect ratios for the larger bubbles obtained in the present study are slightly lower than reported in Colombet et al. (2015) (smaller bubbles) and Ziegenhein and Lucas (2017) ($0.5 < \varphi < 0.6$ for $Eo > 2$), while φ was found to decrease slightly with increasing bubble diameter for $Eo > 2$. More experiments using close-up photographs of the bubble column are needed to further study bubble sizes and shapes, which also requires a very complex image analysis algorithm due to the high density of bubbles in the column.

4. Conclusions

New experiments were performed in a homogeneously sparged rectangular bubble column with large, almost uniformly sized bubbles operated with and without liquid co-flow.

Very uniform void fraction profiles were obtained for U_{sg} up to 3.0 cm/s at void fractions up to ≈14%. A gradual transition to inhomogeneous bubbly flow was observed for larger U_{sg}. Average gas fraction measurements, with and without liquid co-flow, agree very well with the correlation for the overall gas hold-up developed in our previous paper (Muilwijk and Van den Akker, 2019).

Bubble velocities were measured using dual-tip optical fibre probes and compared with parcel velocities obtained using a Bubble Image Velocimetry approach. Very good agreement between both methods was found for gas fractions <5% and U_{sl} up to 0.1 m/s, whereas a < 10% higher velocity was found from BIV measurements compared to OFP measurements for higher U_{sl}. While the biases of (dual-tip) optical fibres are well-known, further research is required to calibrate the BIV method. As the optical fibres are centered in the column between the front and rear wall, while the images for the BIV method are captured of the front column wall, gradients of v_b in co-linear direction may impede a fair comparison of the two methods and further study is required to investigate the possibility of wall peaking gas fractions and bubble velocities.

A liquid co-flow was found to reduce spatial variations of v_b and mitigate the wake effect of the splitter plate, therefore stabilizing a homogeneous bubbly flow. Bubble rise velocities as a function of gas fraction were compared to similar studies and hindered bubble rise was not observed in any case due to the large(r) size of the bubbles.

Very similar bubble chord length distributions were measured along the horizontal position in the column which confirms the uniformity of the bubble size and homogeneous sparging. Mean bubble chord lengths were found to increase with increasing U_{sg} and to decrease with increasing U_{sl} in a similar way as d_{eq} depends on U_{sg} and U_{sl}.

As bubbles do not behave as rigid ellipsoids and intrusive measurements are subjected to measurement biases, an improved method should be developed to distinguish between bubble size (chord) and shape more accurately.

For this Part I paper, we reported accurate data for the effect of liquid co-flow on gas hold-up, bubble velocities and chord lengths, for bubbly flows characterized by large, uniformly sized, bubbles in the range 4–7 mm. Such data may be useful for validating CFD simulations, specifically the Euler-Euler (two-fluid) type, as models for bubble coalescence/breakup and segregated size classes are no longer required. Hence, models for interfacial momentum transfer mechanisms can be validated for a truly uniform bubble size. Future work then may include to study the effect of a bi-modal bubble size distribution, such that terminal rise velocities are no longer similar. Models for lateral dispersion can be properly validated based on empirical knowledge of the bubble size distribution, and depending on the interfacial tension (water type), coalescence could start to play a role.

Our Part II paper will deal with flow patterns in an asymmetrically sparged bubble column with an uneven co-flow by a parametric study using the same dual-tip optical fibre probes and Bubble Image Velocimetry.

Declaration of Competing Interest

The authors declare that they have no known competing financial interests or personal relationships that could have appeared to influence the work reported in this paper.

CRediT authorship contribution statement

Corné Muilwijk: Conceptualization, Methodology, Software, Validation, Formal analysis, Investigation, Writing - original draft, Visualization. **Harry E.A. Van den Akker:** Conceptualization, Writing - review & editing, Supervision, Funding acquisition.

Acknowledgments

This research was made possible through a start-up fund in the context of the Bernal Project at the University of Limerick. We acknowledge Saikat Bhowmick for assistance during the experiments.

Appendix A. Details about chord length distributions

A1. Simulated chord length distributions

Our results (with a uniform, single bubble size) suggest that assuming a constant shape factor when transforming a CLD to a BSD is insufficiently accurate for large bubbles as they behave as non-rigid oblate ellipsoids. To further investigate this, we simulated chord length distributions for uniformly sized bubbles ($d_{eq} = 5$ mm) for non-constant bubble shapes as well as for rigid bubbles of a dispersed size.

$n = 10^3$ random numbers were drawn to represent different aspect ratios or bubble sizes as outlined below:

1. Rigid oblate bubbles of uniform $d_{b,eq}$ with $\varphi = 0.5$ (constant shape);
2. Rigid oblate bubbles ($\varphi = 0.5$) with Gaussian distributed bubble equivalent diameters: $D_{b,eq} = \text{Norm}(5, 0.5)$,
3. Uniform bubbles with a uniformly distributed aspect ratio: $E = \text{U}(0.41, 0.59)$;
4. Uniform bubbles with an arcsinusoidal distributed aspect ratio (φ may exhibit an harmonic motion): $E = \text{Arcsine}(0.43, 0.57)$;
5. Uniform bubbles with a Gaussian distributed aspect ratio: $E = \text{Norm}(0.5, 0.05)$, and
6. Both normally distributed aspect ratios and bubble equivalent diameters: $D_{b,eq} = \text{Norm}(5, 0.5)$ and $E = \text{Norm}(0.5, 0.05)$

where E, D denote the distributions of aspect ratio φ and the bubble equivalent diameter $d_{b,eq}$ respectively. The variance in E (No. 3-5) was kept constant.

Then, for each bubble shape in E (No. 1,3-5) or size in $D_{b,eq}$ (No. 2), two large sets of random numbers (for the two horizontal directions R_x, R_y) proportional to the horizontal diameter (a_i^2) were drawn from a uniform distribution, $\text{U}(-a_i, a_i)$. The chord length distribution for each subset i was then calculated according to:

$$C_i = b_i\sqrt{1 - \left(\frac{R}{a_i}\right)^2} \quad \text{for} \quad R < a_i \tag{A.1}$$

where $R = \sqrt{R_x^2 + R_y^2}$. a_i, b_i are calculated using $d_{b,eq}$ and $\varphi = b_i/a_i$, see Eq. (7).

Fig. A.17 shows the simulated probability density function estimates for the five cases. For uniformly sized rigid bubbles with an aspect ratio of $\varphi = 0.5$, a triangular chord length distribution was recovered (black solid line) with a modal chord length (almost) equal to the maximum chord length (Clark and Turton, 1988). The maximum chord length observed is 3.15 mm, which agrees with $d_{b,eq} = 5$ mm and $E = 0.5$, see Eq. (7).

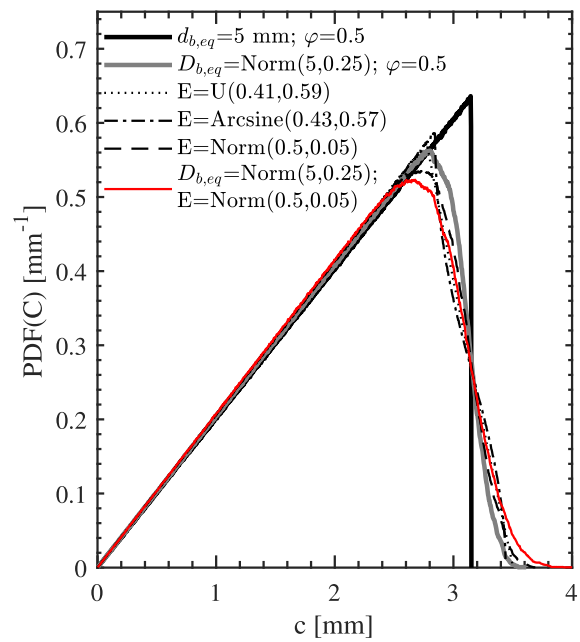

Fig. A.17. Modeled chord length distribution for oblate bubbles of various size and aspect ratio distributions.

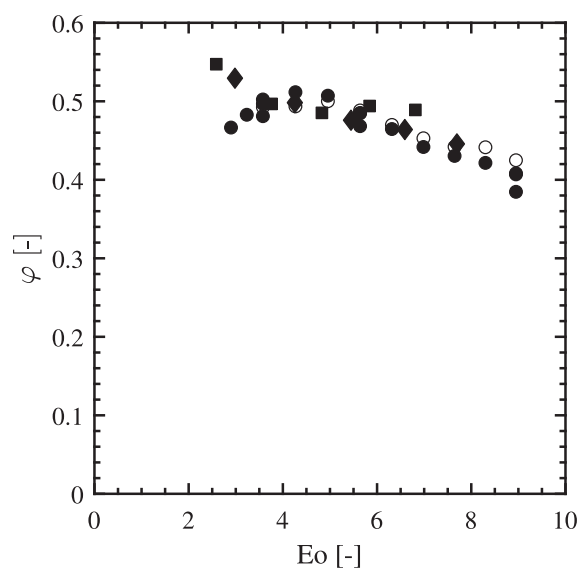

Fig. A.18. Bubble aspect ration φ as a function of *Eo*.

The gray solid line shows the simulated chord length histogram for univariate rigid (geometrically similar, $\varphi = 0.5$) bubbles in $D_{b,eq}$ of an average diameter $\overline{d_{b,eq}} = 5$ mm and a Coefficient of Variation of 5% (which is even larger than obtained experimentally in Muilwijk and Van den Akker (2019)). Due to the dispersity in the (vertical) diameter, the right tail of the distribution is elongated, while the sharp peak at the modal chord length flattened.

For equally sized bubbles with a uniformly distributed aspect ratio in E, a triangular chord length distribution was observed

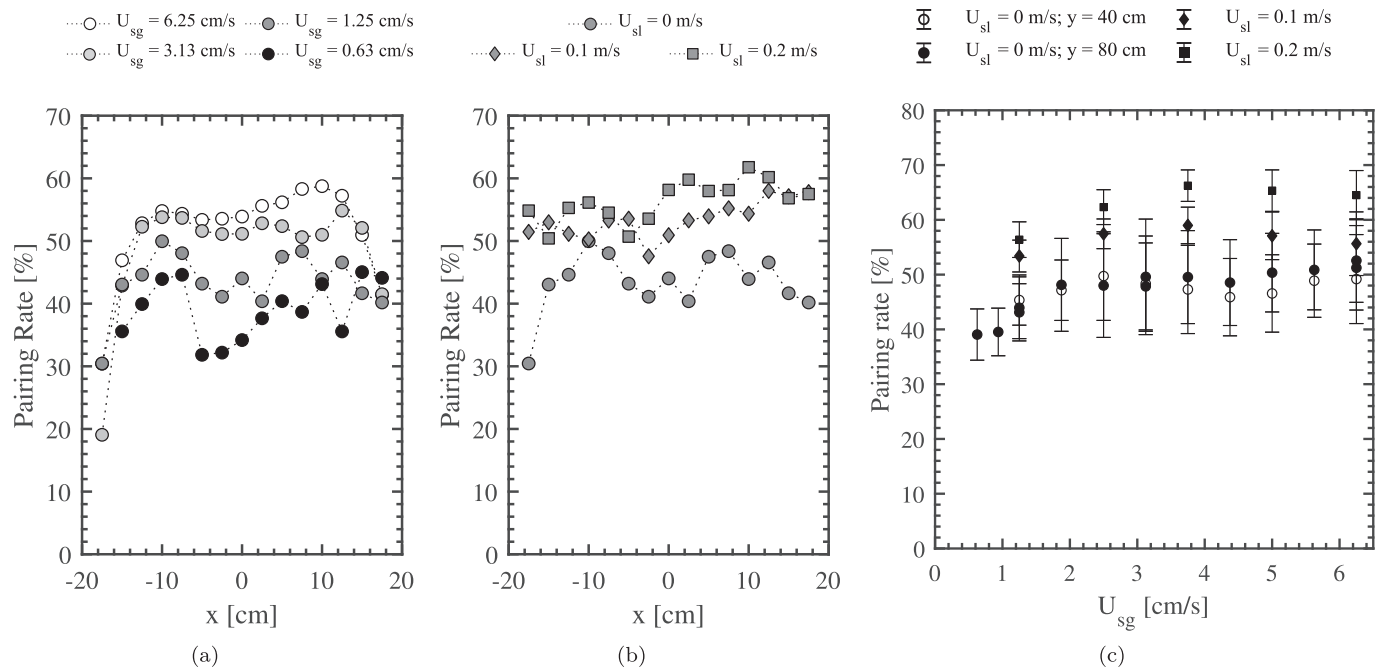

Fig. B.19. (a,b): Pairing rates as a function of x for (a): no co-flow ($U_{sl} = 0$ m/s) and various U_{sg}; and (b): with co-flow ($U_{sl} = 0, 0.1, 0.2$ m/s) for $U_{sg} = 1.25$ cm/s. $y = 80$ cm. (c): Average pairing rates as a function of U_{sg}. The error bars indicate the horizontal spreading. The solid markers show data taken at $y = 80$ cm; the open markers show data for $y = 40$ cm.

(dotted line) with a modal chord length at $\approx 0.8\times$ the maximum chord length. Almost no difference was found between a uniformly and arcsinusoidal (dash-dotted line) distributed aspect ratio.

For a normally distributed aspect ratio (dashed line), the bubble chord length histogram approaches a chord length distribution for a normally distributed bubble size distribution, while the bubbles are uniform in terms of volume equivalent diameter.

The deviation from a triangular chord length distribution, as given by the solid black line in Fig. A.17, can be due to both (1) the non-uniformity of the bubble size; and (2) the non-constant shape in the wobbling regime. We therefore conclude that a chord length distribution cannot be transformed into a bubble size distribution when bubbles exhibit a non-constant shape.

A2. Aspect ratio as a function of the Eötvös number

The bubble aspect ratios are calculated, using Eq. (7), from the mean of the chord length distributions and the volume equivalent bubble diameter, which is given by the correlation developed in our previous paper (Muilwijk and Van den Akker, 2019). The bubble aspect ratio as a function of the Eötvös number ($Eo = \rho_w g d_{b,eq}^2/\sigma$) is given in Fig. A.18. It should be noted that, for $U_{sl} = 0$ m/s and $U_{sg} > 3.5$ cm/s, the bubble size can no longer be assumed as strictly uniform due to coalescence (and breakup) happening at the needle outlets.

Appendix B. Pairing rates

The pairing rates as a function of x, U_{sg} and U_{sl} are given in Fig. B.19. The error bars (c) denote the spreading in lateral (x) direction, the 15 measurement locations as shown in Fig. 1. The pairing rate was almost independent of U_{sg}, but increased from 50% to 65% for U_{sl} in the range 0–0.2 m/s due to (1) increased alignment of the bubble velocity direction and the probe; and (2) the higher inertia of the bubbles' added mass reducing the effect of drifting.

Supplementary material

Supplementary material associated with this article can be found, in the online version, at doi:10.1016/j.ijmultiphaseflow.2020.103498.

References

Van den Akker, H.E.A., 1998. The euler-euler approach to dispersed two-phase flows in the turbulent regime. ERCOFTAC Bull. 36, 30–33.
Alméras, E., Plais, C., Roig, V., Risso, F., Augier, F., 2018. Mixing mechanisms in a low-sheared inhomogeneous bubble column. Chem. Eng. Sci. 186, 52–61. doi:10.1016/j.ces.2018.04.026.
Bai, W., Deen, N., Mudde, R., Kuipers, J., 2008. Accuracy of bubble velocity measurement with a four-point optical fibre probe. In: Proceedings of the 6th International Conference on Computational Fluid Dynamics (CFD) in Oil & Gas, Metallurgical and Process Industries, 10-12 June 2008, Trondheim, Norway. SINTEF/NTNU.
Bai, W., Deen, N.G., Kuipers, J.A.M., 2010. Bubble properties of heterogeneous bubbly flows in a square bubble column. AIP Conf. Proc. 1207 (1), 563–568. doi:10.1063/1.3366427.
Bakker, A., 1992. Hydrodynamics of stirred gas-liquid dispersions. Delft University of Technology, Delft, The Netherlands Ph.D. Thesis.
Barrau, E., Rivière, N., Poupot, C., Cartellier, A., 1999. Single and double optical probes in air-water two-phase flows: real time signal processing and sensor performance. Int. J. Multiph. Flow 25 (2), 229–256. doi:10.1016/S0301-9322(98)00042-1.
Besagni, G., Brazzale, P., Fiocca, A., Inzoli, F., 2016. Estimation of bubble size distributions and shapes in two-phase bubble column using image analysis and optical probes. Flow Meas. Instrum. 52, 190–207. doi:10.1016/j.flowmeasinst.2016.10.008.
Besagni, G., Inzoli, F., 2016. Comprehensive experimental investigation of counter-current bubble column hydrodynamics: holdup, flow regime transition, bubble size distributions and local flow properties. Chem. Eng. Sci. 146, 259–290. doi:10.1016/j.ces.2016.02.043.
Besagni, G., Inzoli, F., Ziegenhein, T., 2018. Two-phase bubble columns: a comprehensive review. Chem Eng. 2 (2), 13. doi:10.3390/chemengineering2020013.
Besagni, G., Inzoli, F., Ziegenhein, T., Lucas, D., 2017. Computational fluid-dynamic modeling of the pseudo-homogeneous flow regime in large-scale bubble columns. Chem. Eng. Sci. 160, 144–160. doi:10.1016/j.ces.2016.11.031.
Buwa, V.V., Ranade, V.V., 2005. Characterization of gas-liquid flows in rectangular bubble columns using conductivity probes. Chem. Eng. Commun. 192 (9), 1129–1150. doi:10.1080/009864490522704.
Cartellier, A., 1992. Simultaneous void fraction measurement, bubble velocity, and size estimate using a single optical probe in gas-liquid two-phase flows. Rev. Sci. Instrum. 63 (11), 5442–5453. doi:10.1063/1.1143416.

Cartellier, A., Barrau, E., 1998. Monofiber optical probes for gas detection and gas velocity measurements: conical probes. Int. J. Multiph. Flow 24 (8), 1265–1294. doi:10.1016/S0301-9322(98)00032-9.
Cartellier, A., Barrau, E., 1998. Monofiber optical probes for gas detection and gas velocity measurements: optimised sensing tips. Int. J. Multiph. Flow 24, 1295–1315. doi:10.1016/S0301-9322(98)00033-0.
Chang, K.-A., Lim, H.-J., Su, C.B., 2003. Fiber optic reflectometer for velocity and fraction ratio measurements in multiphase flows. Rev. Sci. Instrum. 74 (7), 3559–3565. doi:10.1063/1.1578152.
Chaumat, H., Billet-Duquenne, A., Augier, F., Mathieu, C., Delmas, H., 2005. Application of the double optic probe technique to distorted tumbling bubbles in aqueous or organic liquid. Chem. Eng. Sci. 60 (22), 6134–6145. doi:10.1016/j.ces.2005.04.018.
Cheng, W., Murai, Y., Sasaki, T., Yamamoto, F., 2005. Bubble velocity measurement with a recursive cross correlation PIV technique. Flow Meas. Instrum. 16 (1), 35–46. doi:10.1016/j.flowmeasinst.2004.08.002.
Clark, N., Turton, R., 1988. Chord length distributions related to bubble size distributions in multiphase flows. Int. J. Multiph. Flow 14 (4), 413–424. doi:10.1016/0301-9322(88)90019-5.
Clift, R., Grace, J., Weber, M., Weber, M., 1978. Bubbles, Drops, and Particles. Academic Press.
Colombet, D., Legendre, D., Risso, F., Cockx, A., Guiraud, P., 2015. Dynamics and mass transfer of rising bubbles in a homogenous swarm at large gas volume fraction. J. Fluid Mech. 763, 254–285. doi:10.1017/jfm.2014.672.
Deen, N., Solberg, T., Hjertager, B., 2001. Large eddy simulation of the gas-liquid flow in a square cross-sectioned bubble column. Chem. Eng. Sci. 56 (21), 6341–6349. doi:10.1016/S0009-2509(01)00249-4. Proceedings of the 5th International Conference on Gas-Liquid and Gas-Liquid-Solid Reactor Engineering
Dhotre, M.T., Deen, N.G., Niceno, B., Khan, Z., Joshi, J.B., 2013. Large eddy simulation for dispersed bubbly flows: a review. Int. J. Chem. Eng. 2013, 1–22. doi:10.1155/2013/343276.
Dias, S., França, F., Rosa, E., 2000. Statistical method to calculate local interfacial variables in two-phase bubbly flows using intrusive crossing probes. Int. J. Multiph. Flow 26 (11), 1797–1830. doi:10.1016/S0301-9322(99)00111-1.
Enrique Juliá, J., Harteveld, W.K., Mudde, R.F., Van den Akker, H.E.A., 2005. On the accuracy of the void fraction measurements using optical probes in bubbly flows. Rev. Sci. Instrum. 76 (3), 035103. doi:10.1063/1.1862192.
Frijlink, J.J., 1987. Physical aspects of gassed suspension reactors. Delft University of Technology, Delft, The Netherlands Ph.D. thesis.
Gandhi, A.B., Joshi, J.B., 2010. Unified correlation for overall gas hold-up in bubble column reactors for various gas-liquid systems using hybrid genetic algorithm-support vector regression technique. Can. J. Chem. Eng. 88 (5), 758–776. doi:10.1002/cjce.20296.
Garnier, C., Lance, M., Marié, J., 2002. Measurement of local flow characteristics in buoyancy-driven bubbly flow at high void fraction. Exp. Therm. Fluid Sci. 26 (6), 811–815. doi:10.1016/S0894-1777(02)00198-X.
Groen, J., 2004. Scales and structures in bubbly flows. Delft University of Technology, Delft, The Netherlands Ph.D. thesis.
Guet, S., Fortunati, R.V., Mudde, R.F., Ooms, G., 2003. Bubble velocity and size measurement with a four-point optical fiber probe. Part. Part. Syst. Charact. 20 (3), 219–230. doi:10.1002/ppsc.200390028.
Guet, S., Luther, S., Ooms, G., 2005. Bubble shape and orientation determination with a four-point optical fibre probe. Exp. Therma. Fluid Sci. 29 (7), 803–812. doi:10.1016/j.expthermflusci.2005.03.007. Two Phase Flow
Hampel, U., Otahal, J., Boden, S., Beyer, M., Schleicher, E., Zimmermann, W., Jicha, M., 2009. Miniature conductivity wire-mesh sensor for gas-liquid two-phase flow measurement. Flow Meas. Instrum. 20 (1), 15–21. doi:10.1016/j.flowmeasinst.2008.09.001.
Harteveld, W.K., 2005. Bubble columns: Structures or stability?. Delft University of Technology, Delft, The Netherlands Ph.D. thesis.
Hernandez-Alvarado, F., Kleinbart, S., Kalaga, D.V., Banerjee, S., Joshi, J.B., Kawaji, M., 2018. Comparison of void fraction measurements using different techniques in two-phase flow bubble column reactors. Int. J. Multiph. Flow 102, 119–129. doi:10.1016/j.ijmultiphaseflow.2018.02.002.
Hoang, N., Euh, D., Yun, B., Song, C.-H., 2015. A new method of relating a chord length distribution to a bubble size distribution for vertical bubbly flows. Int. J. Multiph. Flow 71, 23–31. doi:10.1016/j.ijmultiphaseflow.2014.12.006.
Huang, Z., McClure, D.D., Barton, G.W., Fletcher, D.F., Kavanagh, J.M., 2018. Assessment of the impact of bubble size modelling in CFD simulations of alternative bubble column configurations operating in the heterogeneous regime. Chem. Eng. Sci. 186, 88–101. doi:10.1016/j.ces.2018.04.025.
Khan, Z., Bhusare, V.H., Joshi, J.B., 2017. Comparison of turbulence models for bubble column reactors. Chem. Eng. Sci. 164, 34–52. doi:10.1016/j.ces.2017.01.023.
Kiambi, S.L., Duquenne, A.-M., Dupont, J.-B., Colin, C., Risso, F., Delmas, H., 2003. Measurements of bubble characteristics: comparison between double optical probe and imaging. Can. J. Chem. Eng. 81 (3-4), 764–770. doi:10.1002/cjce.5450810357.
Lau, Y., Sujatha, K.T., Gaeini, M., Deen, N., Kuipers, J., 2013. Experimental study of the bubble size distribution in a pseudo-2D bubble column. Chem. Eng. Sci. 98, 203–211. doi:10.1016/j.ces.2013.05.024.
Le Corre, J.-M., Hervieu, E., Ishii, M., Delhaye, J.-M., 2003. Benchmarking and improvements of measurement techniques for local-time-averaged two-phase flow parameters. Exp. Fluids 35 (5), 448–458.
Liao, Y., Rzehak, R., Lucas, D., Krepper, E., 2015. Baseline closure model for dispersed bubbly flow: bubble coalescence and breakup. Chem. Eng. Sci. 122, 336–349. doi:10.1016/j.ces.2014.09.042.
Lichti, M., Bart, H.-J., 2018. Bubble size distributions with a shadowgraphic optical probe. Flow Meas. Instrum. 60, 164–170. doi:10.1016/j.flowmeasinst.2018.02.020.
Lim, H.-J., Chang, K.-A., Su, C.B., Chen, C.-Y., 2008. Bubble velocity, diameter, and void fraction measurements in a multiphase flow using fiber optic reflectometer. Rev. Sci. Instrum. 79 (12), 125105. doi:10.1063/1.3053271.
Liu, W., Clark, N., 1995. Relationships between distributions of chord lengths and distributions of bubble sizes including their statistical parameters. Int. J. Multiph. Flow 21 (6), 1073–1089. doi:10.1016/0301-9322(95)00039-Z.
Lucas, G.P., Mishra, R., 2005. Measurement of bubble velocity components in a swirling gas–liquid pipe flow using a local four-sensor conductance probe. Meas. Sci. Technol. 16 (3), 749–758. doi:10.1088/0957-0233/16/3/018.
Mandalahalli, M.M., Wagner, E.C., Portela, L.M., Mudde, R.F., 2020. Electrolyte effects on recirculating dense bubbly flow: an experimental study using X-ray imaging. AIChE J. 66 (1), e16696. doi:10.1002/aic.16696.
Masood, R.M., Delgado, A., 2014. Numerical investigation of the interphase forces and turbulence closure in 3D square bubble columns. Chem. Eng. Sci. 108, 154–168. doi:10.1016/j.ces.2014.01.004.
McClure, D.D., Kavanagh, J.M., Fletcher, D.F., Barton, G.W., 2017. Experimental investigation into the drag volume fraction correction term for gas-liquid bubbly flows. Chem. Eng. Sci. 170, 91–97. doi:10.1016/j.ces.2016.12.066. 13th International Conference on Gas-Liquid and Gas-Liquid-Solid Reactor Engineering
Mizushima, Y., Sakamoto, A., Saito, T., 2013. Measurement technique of bubble velocity and diameter in a bubble column via single-tip optical-fiber probing with judgment of the pierced position and angle. Chem. Eng. Sci. 100, 98–104. doi:10.1016/j.ces.2013.01.046. 11th International Conference on Gas-Liquid and Gas-Liquid-Solid Reactor Engineering
Muilwijk, C., Van den Akker, H.E.A., 2019. The Limerick bubbly flow rig: design, performance, hold-up and mixing pattern. Chem. Eng. Res. Des. 152, 106–122. doi:10.1016/j.cherd.2019.09.021.
Muilwijk, C., Van den Akker, H.E.A., 2019a. Experimental investigation on the bubble formation from needles with and without liquid co-flow. Chem. Eng. Sci. 202, 318–335. doi:10.1016/j.ces.2019.03.026.
Mukherjee, S., Safdari, A., Shardt, O., Kenjereš, S., Van den Akker, H.E.A., 2019. Droplet–turbulence interactions and quasi-equilibrium dynamics in turbulent emulsions. J. Fluid Mech. 878, 221–276. doi:10.1017/jfm.2019.654.
Murzyn, F., Mouaze, D., Chaplin, J., 2005. Optical fibre probe measurements of bubbly flow in hydraulic jumps. Int. J. Multiph. Flow 31 (1), 141–154. doi:10.1016/j.ijmultiphaseflow.2004.09.004.
Ojha, A., Dahhan, M.A., 2018. Investigation of local gas holdup and bubble dynamics using four-point optical probe technique in a split-cylinder airlift reactor. Int. J. Multiph. Flow 102, 1–15. doi:10.1016/j.ijmultiphaseflow.2017.12.001.
Park, S.H., Park, C., Lee, J., Lee, B., 2017. A simple parameterization for the rising velocity of bubbles in a liquid pool. Nuclear Eng. Technol. 49 (4), 692–699. doi:10.1016/j.net.2016.12.006.
Pjontek, D., Parisien, V., Macchi, A., 2014. Bubble characteristics measured using a monofibre optical probe in a bubble column and freeboard region under high gas holdup conditions. Chem. Eng. Sci. 111, 153–169. doi:10.1016/j.ces.2014.02.024.
Prasser, H.-M., Böttger, A., Zschau, J., 1998. A new electrode-mesh tomograph for gas-liquid flows. Flow Meas. Instrum. 9 (2), 111–119. doi:10.1016/S0955-5986(98)00015-6.
Riboux, G., Risso, F., Legendre, D., 2010. Experimental characterization of the agitation generated by bubbles rising at high Reynolds number. J. Fluid Mech. 643, 509–539. doi:10.1017/S0022112009992084.
Roig, V., Suzanne, C., Masbernat, L., 1998. Experimental investigation of a turbulent bubbly mixing layer. Int. J. Multiph. Flow 24 (1), 35–54. doi:10.1016/S0301-9322(97)00046-3.
Rzehak, R., Krauß, M., Kováts, P., Zähringer, K., 2017. Fluid dynamics in a bubble column: new experiments and simulations. Int. J. Multiph. Flow 89, 299–312. doi:10.1016/j.ijmultiphaseflow.2016.09.024.
Shen, X., Nakamura, H., 2014. Spherical-bubble-based four-sensor probe signal processing algorithm for two-phase flow measurement. Int. J. Multiph. Flow 60, 11–29.
Shen, X., Sun, H., Deng, B., Hibiki, T., Nakamura, H., 2016. Gas-liquid bubbly flow structure in a vertical large-diameter square duct. Prog. Nuclear Energy 89, 140–158.
Shen, X., Sun, H., Deng, B., Hibiki, T., Nakamura, H., 2017. Experimental study on interfacial area transport of two-phase bubbly flow in a vertical large-diameter square duct. Int. J. Heat Fluid Flow 67, 168–184.
Simonnet, M., Gentric, C., Olmos, E., Midoux, N., 2007. Experimental determination of the drag coefficient in a swarm of bubbles. Chem. Eng. Sci. 62 (3), 858–866. doi:10.1016/j.ces.2006.10.012.
Singh, B.K., Quiyoom, A., Buwa, V.V., 2017. Dynamics of gas-liquid flow in a cylindrical bubble column: comparison of electrical resistance tomography and voidage probe measurements. Chem. Eng. Sci. 158, 124–139. doi:10.1016/j.ces.2016.10.006.
Sun, H., Kunugi, T., Shen, X., Wu, D., Nakamura, H., 2014. Upward air–water bubbly flow characteristics in a vertical square duct. J. Nuclear Sci. Technol. 51 (3), 267–281.
Tyagi, P., Buwa, V.V., 2017. Experimental characterization of dense gas-liquid flow in a bubble column using voidage probes. Chem. Eng. J. 308, 912–928. doi:10.1016/j.cej.2016.09.026.

Van den Akker, H.E.A., 1998. Coherent structures in multiphase flows. Powder Technol. 100 (2-3), 123–136. doi:10.1016/S0032-5910(98)00133-8.

Van Den Akker, H.E.A., 2015. Chapter six - mesoscale flow structures and fluid-particle interactions. In: Marin, G.B., Li, J. (Eds.), Mesoscale Modeling in Chemical Engineering Part I. In: Advances in Chemical Engineering, 46. Academic Press, pp. 281–354. doi:10.1016/bs.ache.2015.10.010.

Xue, J., Al-Dahhan, M., Dudukovic, M.P., Mudde, R.F., 2003. Bubble dynamics measurements using four-point optical probe. Can. J. Chem. Eng. 81 (3-4), 375–381. doi:10.1002/cjce.5450810306.

Ziegenhein, T., Lucas, D., 2017. Observations on bubble shapes in bubble columns under different flow conditions. Exp. Therm. Fluid Sci. 85, 248–256. doi:10.1016/j.expthermflusci.2017.03.009.

Zuiderveld, K., 1994. Contrast Limited Adaptive Histogram Equalization. Academic Press Professional, Inc., USA, pp. 474–485.